A Kinetic-Based Model for High-Speed, Monodisperse, Fluid-Particle Flows

Victor Boniou, Rodney O. Fox, Frédérique Laurent

A Kinetic-Based Model for High-Speed, Monodisperse, Fluid–Particle Flows

Victor Boniou[a], Rodney O. Fox[a,b], Frédérique Laurent[b]

[a]*Department of Chemical and Biological Engineering, Iowa State University, Ames, IA 50011-1098, USA*
[b]*Laboratoire EM2C, CNRS, CentraleSupélec, Université Paris-Saclay, 3 rue Joliot-Curie, 91192 Gif-sur-Yvette, France*

Abstract

First, a novel mesoscale kinetic model is developed for monodisperse particles that accounts for collisional and frictional pressures in the dense regime, as well as added mass and internal energy. Then, macroscale particle-phase transport equations for the velocity moments up to second order (i.e., total kinetic energy) are derived from the mesoscale model and closed using a Maxwellian distribution for the particle velocity. When combined with the fluid-phase equations, the system of hyperbolic conservation equations accounts for fully compressible, monodisperse, fluid–particle flows with added mass and fluid-phase pseudoturbulence. The resulting macroscale model is well-posed for any fluid–particle material density ratio. The numerical methods associated with the hyperbolic system are designed to fulfill the main features of a compressible two-phase flow solver: capturing sharp particle fronts, preserving contact discontinuities, and ensuring stability in all flow regimes. This is done by employing a combination of an AUSM$^+$up scheme for the particle phase, and a HLLC scheme for the fluid phase with limited WENO5 reconstructions. Stability is obtained by keeping the discrete consistency between spatial fluxes and non-conservative terms. Test cases combining a high-speed fluid interacting with heavy/light particles are used to demonstrate that the qualitative behavior of the flow dynamics over a wide range of density ratios is captured correctly by the macroscale model.

Keywords: fluid–particle flow, multiscale modeling, kinetic theory of granular flow, added mass, pseudoturbulence, well-posed macroscale model

1. Introduction

High-speed flows in the presence of a particle phase occur in numerous natural and industrial problems such as volcanic ash plumes [45], dust explosions [14], or rocket propulsion [12]. The complexity of such multiphase flows stems from the interaction between the shock and the particles, which highly depends on the volume fraction [56]. While dilute mixtures can be approximated with experiments and numerical simulations of isolated particles subject to a shock, the presence of neighboring particles cannot be neglected when their volume fraction increases [35]. In denser mixtures, a particle is not only subject to the incident shock wave, but also to shock reflections and expansion waves coming from the other particles and compaction waves transmitted through the granular phase. When the mixture becomes very dense, the particles are always in contact and the inter-particle interactions become dominant. The proper modeling of granular flows requires to handle these three regimes with an appropriate physical description. Since the pioneering experiments on a gas-shock interaction with particle curtains [46], both numerical and experimental studies have been conducted to give a better description of the shock-induced dispersal of particles. More specifically, experimental studies have been dedicated to the definition of a universal scaling of the spreading rate with respect to material properties, Mach number, and particle concentration [11, 13, 51]. These works have been followed up by numerical studies to assess different multiphase flow models [28, 35, 41]. More recently, these studies have been extended to hypersonic flows [54] and underwater shocks [2].

In this work, we first propose a novel mesoscale model for the particles in the form of a kinetic equation. This model accounts for collisional particle flow with added mass and internal energy and is consistent with the kinetic

Email addresses: boniouv@iastate.edu (Victor Boniou), rofox@iastate.edu (Rodney O. Fox), frederique.laurent@centralesupelec.fr (Frédérique Laurent)

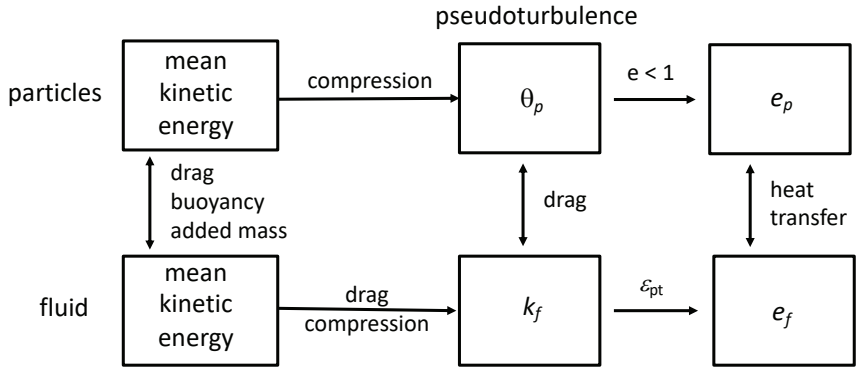

Figure 1: Energy flow in fluid–particle, two-fluid model for monodisperse particles. Spatially uncorrelated particle motion is measured by Θ_p, while particle-scale, fluid-phase, fluctuating kinetic energy is measured by k_f. The internal energies are e_p and e_f. Inelastic collisions transform Θ_p into an increase in e_p. Pseudoturbulent dissipation ε_{pt} transform k_f into an increase in e_f. At each scale, the phases are coupled through drag and heat transfer, and a drag correlation and the Nusselt number are important inputs to the two-fluid model.

theory of granular flows (KTGF). However, for high-speed systems the thermal energy balance must be carefully modeled (e.g., collisional and frictional heating of the particles), which requires terms that are usually neglected in the KTGF for low-speed flows. For clarity, we consider monodisperse, spherical particles with arbitrary material density and identical physical properties so that only the particle number density function (NDF) for velocity and internal energy is needed in the kinetic model. In most applications, the fluid will either be a gas interacting with high-density solid particles or a liquid interacting with low-density particles (e.g., bubbles). For simplicity, we assume that the particle material density remains constant, which implies that the particle volume is constant. Nonetheless, the extension to allow for the particle material density (and hence the volume) to vary with the fluid pressure is straightforward provided that the particle Stokes number for such cases is small (i.e., bubbly flow). The resulting mesoscale model is valid from the very dilute to the very dense regime (as measured by the particle-phase volume fraction). However, for denser flows the particle–particle interaction terms are dominant and the computational cost of solving the kinetic model directly is prohibitive (and often unnecessary).

A tractable macroscale model for denser flows can be derived from the mesoscale model by considering the moments of the NDF as the macroscale conserved variables. As in the kinetic theory of gases, this process introduces mathematical closures for nonlinear terms based on approximating the shape of the NDF. In the macroscale model, the particle-phase equations for the conserved moments are coupled with modified Euler equations for the fluid phase, including pseudoturbulent kinetic energy (PTKE) [49]. Due to the high-speed nature of the flow, viscous terms are neglected but can easily be included when needed [32]. Details on the derivation of the forces and fluxes in the monodisperse two-fluid model can be found in prior work [18, 22, 33]. The fluid phase is treated as inviscid with coupling terms discussed in [22], and the stiffened gas equation of state is used for the fluid pressure. Particle velocity moments up to second order (total kinetic energy) are included, which is sufficient for dense collisional flows [17]. The macroscopic model then accounts for conservation of mass, momentum and total energy for both phases.

In this work, the fluid material density is denoted by ρ_f, and the solids material density (assumed to be constant) is ρ_p. In the macroscale model, the fluid- and particle-phase velocities are $\mathbf{u}_f$ and $\mathbf{u}_p$, respectively. The total energies of the fluid and particle phases are denoted as E_f and E_p, respectively. The total energy is made up of kinetic and internal energies. We denote the former for each phase as K_f and K_p, and the latter as e_f and e_p; hence,

$$E_f = K_f + e_f, \quad E_p = K_p + e_p. \tag{1}$$

The kinetic energy is further divided into mean and fluctuating components (see fig. 1):

$$K_f = \frac{1}{2}u_f^2 + k_f, \quad K_p = \frac{1}{2}u_p^2 + \frac{3}{2}\Theta_p. \tag{2}$$

Here, $u^2 = \mathbf{u}\cdot\mathbf{u}$, k_f is the PTKE, and Θ_p is the granular temperature. The former represents fluid-velocity fluctuations due to finite-size particles, and the square root of the latter represents the velocity magnitude of individual particles relative to $\mathbf{u}_p$. In the macroscale model, the total energy of both phases is conserved. For the fluid phase, it is convenient to solve transport equations for E_f and k_f, and to find e_f from eq. (1). In contrast, for the particle phase, the mesoscale description leads naturally to transport equations for K_p and e_p, and then Θ_p is found from eq. (2). In any case, the thermodynamic temperatures T_f and T_p are found from the internal energies e_f and e_p, respectively.

The diagram in fig. 1 provides a schematic on how kinetic energy is distributed at the macroscale in the fluid–particle flow. The mean kinetic energy is found from the phasic velocities appearing in the momentum balances. Due to their finite size, particles have wakes produced by the slip velocity whose characteristic length scale is proportional to the particle diameter. These wakes interact with individual particles to generate uncorrelated velocity fluctuations measured by the granular temperature [17]. This kinetic energy is dissipated to yet smaller scales to modify the internal energy of both phases. In the absence of body forces (e.g., gravity), the total energy of the two phases is a conserved quantity, and it must be treated as such in the two-fluid model. In a closed system, the total energy at mechanical equilibrium will reside in the internal energies, such that the thermodynamics temperatures of both phases are equal.

The remainder of this paper is organized as follows. In section 2, the mesoscale model for the particles is developed in the form of a kinetic equation that includes the added mass. Unlike in previous work [22] where the added mass was included at the macroscale, the kinetic model accounts for the NDF of the particles. In section 3, the new kinetic model is used to derive a macroscopic model based on the moments of the mass-weighted NDF, which is very similar to the two-fluid model in [22]. In section 4, we present the balance equations for the fluid phase developed in [22] and then in section 4.2 we provide the system of hyperbolic equations for the macroscale model. In section 5, we present a robust numerical algorithm for solving the model equations (which include the added mass) for arbitrary material-density ratios ranging from bubbly liquids to gas–particle flows. Section 6 is devoted to 1-D numerical examples using flow conditions taken from the literature. Finally, in section 7, conclusions are drawn and possible extensions to low-Mach-number and combusting flows are discussed.

2. Mesoscale model for monodisperse particles with added mass

To account for the added mass and the particle pressure due to collisions and friction in a simplified, but accurate, manner, at the mesoscale we use a kinetic-based model for the particles [40]. At the kinetic level, individual particles with different velocities $\mathbf{u}$ and internal energies e are represented by a NDF, denoted by $n(t, \mathbf{x}, \mathbf{u}, e)$, the moments of which contain information such as the mass, momentum and kinetic energy of the particle phase.[1] The internal energy of a particle moves with velocity $\mathbf{u}$, and is accounted for as an internal variable. When needed, the chemical composition of the particles is handled in the same manner as internal energy [40].

In summary, $n(\mathbf{u}, e)\,\mathrm{d}\mathbf{u}\,\mathrm{d}e$ is the average number of particles with velocity $\mathbf{u}$ and internal energy e. Letting V_p denote the (constant) particle volume, the first three moments of this NDF:

$$\alpha_p = \int V_p n(\mathbf{u}, e)\,\mathrm{d}\mathbf{u}\,\mathrm{d}e, \quad \alpha_p\mathbf{u}_p = \int \mathbf{u} V_p n(\mathbf{u}, e)\,\mathrm{d}\mathbf{u}\,\mathrm{d}e, \quad \alpha_p e_p = \int e V_p n(\mathbf{u}, e)\,\mathrm{d}\mathbf{u}\,\mathrm{d}e, \tag{3}$$

define the particle-phase volume fraction α_p, velocity $\mathbf{u}_p$, and internal energy e_p, respectively. The mesoscale model is a closed kinetic equation for the NDF. Thus, in principle, it can be solved to find $n(t, \mathbf{x}, \mathbf{u}, e)$ given the initial conditions $n(0, \mathbf{x}, \mathbf{u}, e)$. In previous applications of kinetic-based models to fluid–particle systems, the added-mass contribution has been neglected. This assumption is reasonable for gas–solid systems, but not for liquid–solid nor bubbly flows. Thus, before introducing the kinetic model, we first describe how added mass can be treated at the mesoscale.

2.1. Treatment of added mass at the mesoscale

In our modeling approach [10, 22], added mass is handled by assigning a fraction of the fluid phase surrounding a particle to move with the velocity of the particle. In the context of two-fluid models, we define $\alpha_p^\star = \alpha_p + \alpha_a$ where

[1] In this context, "phase balance" means a balance over the ensemble of all particles. Thus, information concerning individual particles is lost, but classical conservation of mass, momentum and energy still hold.

α_a is the volume fraction of the added-mass phase while α_p is the particle-phase volume fraction. In the absence of particles, both α_p and α_a are null. It then follows that $\alpha_f^\star = \alpha_f - \alpha_a$ where α_f is the fluid-phase volume fraction. As usual, the volume fractions are non-negative with $\alpha_p + \alpha_f = 1$ and $\alpha_p^\star + \alpha_f^\star = 1$. The (constant) mass of a particle is denoted by $m_p = \rho_p V_p$, whereas the particle mass + added mass is denoted by $m_p^\star = \beta(t, \mathbf{x}) m_p$ where $\beta(t, \mathbf{x})$ is the added-mass factor defined below and is the same for every particle located at $\mathbf{x}$ at time t. With this definition for the particle mass, we now define the mass density function (MDF) as $f(t, \mathbf{x}, \mathbf{u}, e) = m_p^\star n(t, \mathbf{x}, \mathbf{u}, e)$. The kinetic model in section 2.2 will be based on the MDF. By integrating over the variables $(\mathbf{u}, e)$, the relation between the NDF and the MDF yields the identity $\rho_e \alpha_p^\star = \beta \rho_p \alpha_p$, which defines the effective particle density ρ_e. An equivalent definition for ρ_e that is used in the numerical solver is

$$\rho_e = \frac{\alpha_p}{\alpha_p^\star}(\rho_p - \rho_f) + \rho_f \tag{4}$$

where $\alpha_p \le \alpha_p^\star$. Note that solving for any two of the three quantities $(\beta, \rho_e \alpha_p^\star, \rho_p \alpha_p)$ determines all three. For convenience, in the macroscale model in section 3, we will solve for $(\rho_e \alpha_p^\star, \rho_p \alpha_p)$ and use eq. (4) to compute $\rho_e(t, \mathbf{x})$.

The transport equation for the added-mass factor $\beta(t, \mathbf{x}) \ge 1$ is

$$\partial_t \beta + \mathbf{u}_p \cdot \partial_{\mathbf{x}} \beta = \frac{1}{\tau_a}(\beta^\star - \beta) \tag{5}$$

where $\mathbf{u}_p$ is the particle-phase velocity found from the MDF. Physically, the added-mass factor is transported with the particle-phase velocity and relaxes towards the local equilibrium value. The timescale for relaxation towards equilibrium τ_a is assumed to be proportional to the timescale for single-particle drag τ_p, i.e., $\tau_a \lessapprox \tau_p$. In a spatially homogeneous system, starting with $\beta(0) = 1$, eq. (5) causes $\beta(t)$ to relax exponentially towards $\beta^\star$, i.e., the added mass is initially zero and relaxes to $m_p^\star - m_p$ with characteristic timescale τ_a.

If we write the added-mass volume fraction as $\alpha_a = c_m \alpha_f \alpha_p$ where $0 < c_m(t, \mathbf{x}) < 1$ is the added-mass coefficient with equilibrium value $c_m^\star$, then β and $\beta^\star$ are related to c_m by

$$\beta = 1 + \frac{\rho_f}{\rho_p} c_m \alpha_f, \quad \beta^\star = 1 + \frac{\rho_f}{\rho_p} c_m^\star \alpha_f. \tag{6}$$

In this work, the default value of the added-mass coefficient $c_m^\star$ is set to

$$c_m^\star = \frac{1}{2} \min(1 + 2\alpha_p, 2), \tag{7}$$

and hence $\beta^\star(t, \mathbf{x})$ depends on the material density ratio $\rho_f(t, \mathbf{x})/\rho_p$ and $\alpha_p(t, \mathbf{x})$. For very dilute flows, $c_m^\star = \frac{1}{2}$ as expected for spherical particles.

Physically, the added mass represents the fluid surrounding a particle, also moving with velocity $\mathbf{u}$ [10, 22], but the individual particle's added volumes are strongly coupled together through β, which moves with velocity $\mathbf{u}_p$. Thus, heat and/or mass transfer to (from) the particle phase from (to) the fluid phase passes through the added volume. For simplicity, here we will assume that the internal energy of the particle + added mass (denoted by e) is uniform in the particle, leading to a single temperature T.[2] This assumption is compatible with [28], and is used to define the temperature difference $T - T_f$ that drives heat transfer between a particle and the surrounding fluid.

2.2. Kinetic model

The MDF is proportional to the average mass of particles (including added mass) at space–time location $(\mathbf{x}, t)$ with phase-space properties $(\mathbf{u}, e)$. Thus, at the mesoscale, each particle has its own velocity $\mathbf{u}$ and internal energy e, but

[2]The effective heat capacity of the particle + added mass can be approximated using the heat capacities of the fluid and solid weighted by α_a and α_p, respectively.

otherwise the particle properties are identical. The proposed kinetic model for the MDF has the following form:

$$\partial_t f + \partial_{\mathbf{x}} \cdot \left(\mathbf{u} f - P_p \frac{\partial f}{\partial \mathbf{u}} \right) + \frac{\partial}{\partial \mathbf{u}} \cdot \left[\mathbf{A}_u f - \frac{1}{\rho_e} (\partial_{\mathbf{x}} \hat{p}_f + \mathbf{F}_{pf}) f - \frac{1}{\rho_e \alpha_p^\star} (\partial_{\mathbf{x}} \cdot \mathbf{P}_{pfp}) f \right] + \frac{\partial}{\partial e} (A_e f) = \frac{\partial^2}{\partial \mathbf{u} \partial \mathbf{u}} : (\mathbf{B}_u f) + C + F + S. \quad (8)$$

It is important to note that eq. (8) is closed, meaning that it can be solved for the MDF. However, because of the high dimensionality of the MDF (i.e., eight independent variables in 3-D), a direct-numerical solution is computationally expensive. For this reason, in section 3 the kinetic model is used to derive a macroscale model for moderately dense to dense flows with fewer variables. Nonetheless, for very dilute flows it will necessary to solve eq. (8) directly using, for example, Euler–Lagrange methods [7].

As discussed below, many of the terms in the kinetic model are coupled to the fluid-phase variables. Thus, the kinetic model in eq. (8) and the modified Navier–Stokes equation for the fluid are coupled, and must be solved together in order to find the MDF. In the following, we will describe the model for and the physical meaning of each of the terms appearing in eq. (8).

2.2.1. Free transport

The free-transport of particles corresponds to $\partial_t f + \mathbf{u} \cdot \partial_{\mathbf{x}} f = 0$. In a Lagrangian simulation, this term gives $\mathrm{d}\mathbf{x}/\,\mathrm{d}t = \mathbf{u}$, but is the most difficult term to handle in a macroscale model [20]. In the particle-phase momentum balance, it produces that kinetic pressure due to particles with different velocities. For dilute flow ($\alpha_p < 0.001$), the particle-phase speed of sound due to the kinetic pressure scales like $\sqrt{3\Theta_p}$.

2.2.2. Pressure terms

The particle-phase pressure $P_p = P_c + P_{fr}$ arises due to particle–particle interactions in the KTGF [40]. The model depends on the velocity moments up to second order [18], and is the sum of a collisional component:

$$P_c = 2(1 + e_c)\alpha_p g_0 \Theta_p \quad \text{with} \quad g_0 = \frac{1 + \alpha_f}{2\alpha_f^3} \quad (9)$$

where e_c is the coefficient of restitution; and a frictional (or close-packed) component, modeled here as

$$P_{fr} = \frac{p_{fr} \alpha_p g_0}{\rho_e \alpha_p^\star} h_{fr} \quad \text{with} \quad h_{fr} = \frac{1}{2} \left[1 + \tanh \left(\frac{\alpha_p - \alpha_{max}}{\Delta_{fr}} \right) \right] \quad (10)$$

where α_{max} is the close-packed limit and Δ_{fr} controls the sharpness of the transition to α_{max}. The parameter p_{fr} fixes the speed of sound in the particle phase above the close-packed limit. The functional form of h_{fr} causes P_{fr} to rapidly increase from zero near $\alpha_p = \alpha_{max} \approx 0.63$.

In general, the functional form for P_{fr} must ensure that the frictional pressure increases monotonely with volume fraction, i.e., $d\rho_e \alpha_p^\star P_{fr}/d\alpha_p > 0$. In general, if $\alpha_p < 0.001$ (dilute regime), then P_p is negligible. Finally, note that added mass plays no role in $\rho_e \alpha_p^\star P_{fr}$ because the particles are in contact. Other forms for P_c that account for velocity correlations between colliding particles are also available [30]. Here, for clarity, when the particle pressure depends on both α_p and Θ_p, we refer to it as collisional; otherwise, when it depends only on α_p, we refer to it as frictional. In any case, although it is negligible for very dilute flows, P_p controls the particle-phase speed of sound for dense flows.

2.2.3. Acceleration terms

In eq. (8), for the fluid-drag term, the acceleration vector $\mathbf{A}_u$ has the form

$$\mathbf{A}_u = \frac{\mathbf{u}_f - \mathbf{u}}{\tau_p} \quad (11)$$

where τ_p is the drag timescale that depends on α_p and $\mathbf{u}_{pf}$:

$$\tau_p = \tau_p = \frac{4\rho_e d_p^2}{3\mu_f C_D Re_p} = \frac{4}{3}\frac{\alpha_f}{\alpha_f^\star}\beta\frac{\rho_p d_p^2}{\mu_f C_D Re_p} \tag{12}$$

and the particle Reynolds number is

$$Re_p = \frac{\rho_f d_p v_{pf}}{\mu_f}. \tag{13}$$

In the definition of Re_p, the slip velocity v_{pf} is defined in the absence of added mass (i.e., $\beta = 1$, $\alpha_f^\star = \alpha_f$). As shown in [22], the slip velocities with and without added mass are related by $\alpha_f \mathbf{v}_{pf} = \alpha_f^\star \mathbf{u}_{pf}$. The slip velocity with added mass is larger because part of the fluid moves with the particle velocity $\mathbf{u}_p$. However, drag models in the literature are based on v_{pf}, so that τ_p in eq. (12) is multiplied by $\alpha_f/\alpha_f^\star$ to recover the correct drag force. Here, d_p is the particle diameter and C_D is a drag coefficient that depends on the particle Reynolds number and other dimensionless parameters such as the Mach number and volume fraction. For Stokes flow, which is valid for very small particles and $\alpha_f = 1$, $C_D Re_p = 24$.

The buoyancy force in eq. (8) $(f/\rho_e)\partial_{\mathbf{x}}\hat{p}_f$ depends on the gradient of the modified fluid pressure. The latter is defined by $\hat{p}_f = p_f + \frac{2}{3}k_f$ where p_f is the thermodynamic pressure and k_f is the PTKE. In most flows, $p_f \gg k_f$. The buoyancy force must be included in moderately dense and dense flows in order to get the correct eigenvalues for the fluid-phase spatial flux. Moreover, because it scales with the fluid density, buoyancy is very important in liquid–solid and bubbly flows.

In eq. (8), we treat the particle–fluid force $\mathbf{F}_{pf}$ and the particle–fluid–particle (pfp) pressure tensor $\mathbf{P}_{pfp}$ as independent of $\mathbf{u}$; however, this is not a requirement. The particle–fluid force $\mathbf{F}_{pf}$ arises due to finite-size particles [22], and is the same as when added mass is neglected. For a monodisperse system, it was derived from kinetic theory [18] by accounting for the excluded volume of the particles:

$$\mathbf{F}_{pf} = \mathbf{R}\cdot\partial_{\mathbf{x}}\rho_f - \frac{2}{3}\rho_f tr(\mathbf{\Gamma})\,\mathbf{u}_{pf} - \frac{4}{5}\rho_f \mathbf{S}\cdot\mathbf{u}_{pf} \quad \text{with} \quad \mathbf{R} = \frac{1}{5}u_{pf}^2\mathbf{I} + \frac{2}{5}\mathbf{u}_{pf}\otimes\mathbf{u}_{pf} \tag{14}$$

where the fluid-phase deformation rate tensor is $\mathbf{\Gamma} = \frac{1}{2}\left[\partial_{\mathbf{x}}\mathbf{u}_f + (\partial_{\mathbf{x}}\mathbf{u}_f)^t\right]$ and $\mathbf{S} = \mathbf{\Gamma} - \frac{1}{3}tr(\mathbf{\Gamma})\mathbf{I}$. The term $\mathbf{R}\cdot\partial_{\mathbf{x}}\rho_f$ can be important when strong shocks are present, i.e., where the fluid density changes rapidly. The second term in $\mathbf{F}_{pf}$ modifies the fluid drag when $0 < |\partial_{\mathbf{x}}\cdot\mathbf{u}_f|$, while the third term represents lift. The latter was derived considering only mean gradients of density and velocity in a compressible flow [18], and should be replaced by a lift model accounting for the particle Reynolds number [28]. In practice, in high-speed flows $\mathbf{F}_{pf}$ can have the same order of magnitude as the buoyancy force.

Notice that $tr(\mathbf{R}) = u_{pf}^2$, which can be very large in high-speed flows. In the mesoscale model, $\mathbf{F}_{pf}$ can be made dependent on $\mathbf{u}$ by replacing $\mathbf{u}_{pf}$ by $(\mathbf{u} - \mathbf{u}_f)$. If this is done for $\mathbf{R}$, its trace will be larger due to a contribution proportional to Θ_p [18]. For moderately dense to dense flows, the velocity distribution function (VDF) is mainly determined by collisions and fluid drag. Thus, making such a change to $\mathbf{F}_{pf}$ will have a negligible effect on the results. However, in very dilute cases, the effect would be more significant since $|\mathbf{u} - \mathbf{u}_f|$ is much larger than u_{pf} in the tails of the VDF. Moreover, in such cases the tails of the VDF may be far from Gaussian. Nevertheless, the macroscale model will not be valid in very dilute cases.

The pfp-pressure tensor described in [22] can be modeled as

$$\mathbf{P}_{pfp} = C_{pfp}\rho_f\alpha_p^\star\mathbf{R} \tag{15}$$

with $C_{pfp} = c_m^\star$ ensuring hyperbolicity when $\rho_p \ll \rho_f$ (e.g., bubbly flows). We should note that this term has physical relevance for freely moving particles, i.e., below the close-packed limit. However, above close packing, its contribution will be very small compared to fluid drag. Nonetheless, it is important for the particle phase, particularly in dilute cases, and in high-speed flows with a large slip velocity or steep volume-fraction gradients (e.g., a shock hitting a particle curtain).

Recently [55], the pfp-stress tensor $\mathbf{\Sigma}_{pfp}$ $(= -\mathbf{P}_{pfp})$ has been computed for fixed particles $(\Theta_p = 0)$ in an incom-

pressible fluid. These authors found that the pfp-pressure tensor has the form

$$\mathbf{P}_{pfp} = \rho_f \alpha_p^\star [B_1(\alpha_p, Re_p)\, u_{pf}^2 \mathbf{I} + B_2(\alpha_p, Re_p)\, \mathbf{u}_{pf} \otimes \mathbf{u}_{pf}] \tag{16}$$

with positive trace, and they provide correlations for B_1 and B_2 over limited ranges of α_p and Re_p. For example, they find that B_1 has a weak dependence on α_p (i.e., $-0.01 \ln \alpha_p$) and B_2 is nearly independent of α_p. More generally, the tensor form in eq. (16) is unique for systems without macroscopic gradients [55]. It may therefore be reasonable to use B_1 and B_2 in eq. (16) to redefine the coefficients in $\mathbf{R}$ (i.e., replacing 1/5 and 2/5, respectively) such that C_{pfp} in eq. (15) is defined by enforcing $tr(\mathbf{R}) = u_{pf}^2$. In any case, for the one-dimensional (1-D) flows investigated in this work, only $tr(\mathbf{P}_{pfp}) = C_{pfp}\rho_f \alpha_p^\star u_{pf}^2$ is required.

The velocity diffusion term on the right-hand side of eq. (8) with coefficient matrix

$$\mathbf{B}_u = \frac{1-a}{\tau_p}\left((\mathbf{u}-\mathbf{u}_p)\otimes(\mathbf{u}-\mathbf{u}_p) + \frac{2}{3}k_f\mathbf{I}\right) \qquad \Longrightarrow \qquad tr(\mathbf{B}_u) = \frac{1-a}{\tau_p}(|u-u_p|^2 + 2k_f) \tag{17}$$

is due to fluid-phase PTKE accelerating the particles relative to their mean velocity with drag timescale τ_p. In $tr(\mathbf{B}_u)$, the total fluctuating energy in both phases is $|u-u_p|^2+2k_f$, so that the parameter a controls the amount transferred to the particles. If PTKE anisotropy were accounted for in the model [19], $2k_f/3\mathbf{I}$ would be replaced by the PTKE Reynolds-stress tensor. The parameter a depends on the material densities, and is modeled as

$$\frac{1-a}{1-a_{min}} = \frac{\rho_f}{\rho_p K + \rho_f} \tag{18}$$

where $a_{min} = 0.5$ determines the steady-state ratio Θ_p/k_f for gas bubbles in a liquid (i.e., $\rho_p/\rho_f \ll 1$), and $K = 0.06$ fixes the steady-state ratio for $\rho_f = \rho_p$. Heavy particles in a gas correspond to $a \lessapprox 1$.

Note that in an Euler–Lagrange simulation of eq. (8) the acceleration terms inside $\partial/\partial\mathbf{u}$ would be applied to each particle separately. Likewise, the square-root matrix found from non-negative, symmetric matrix $\mathbf{B}_u$ would define the coefficient matrix for a random acceleration of each particle driven by a Wiener process.

2.2.4. Heat-transfer term

The term in eq. (8) involving A_e accounts for exchange of particle internal energy e with the fluid phase due to the temperature difference. Denoting the particle temperature by T, which is in a one-to-one relation with e, we can define this term by

$$A_e = \frac{6\lambda_f Nu}{\rho_e d_p^2}(T_f - T) \tag{19}$$

where the phase temperatures are found from their internal energies. Hereinafter, for simplicity, we will take the heat capacities as constant such that

$$T_f = \frac{\gamma_f e_f}{C_{p,f}}, \qquad T = \frac{e}{C_{p,p}}. \tag{20}$$

This assumption will be valid as long as the temperatures do not vary too much. The Gunn correlation [26] for the Nusselt number (Nu) is given in [28] and table 2, and λ_f is the fluid-phase thermal conductivity.

2.2.5. Collisional source term

The mesoscale models for particle–particle interactions are based on hard-sphere collisions via the Enskog–Boltzmann equation [40]. Here, since the internal energy is included in the MDF, and e changes due to inelastic collisions, we must define exactly how e changes during a collision event. The microscale (particle-level) model for binary collisions has the following properties. Let $(\mathbf{u}, e)_1, (\mathbf{u}, e)_2$ be the particle velocities and internal energies before a collision, and $(\mathbf{u}', e')_1, (\mathbf{u}', e')_2$ be the values after collision. Because collisions are Galilean invariant, a frame of reference with zero mean velocity can be chosen such that $\mathbf{u}_1$ and $\mathbf{u}_2$ correspond to fluctuating velocities with respect to the mean velocity of the particle pair. Then, for monodisperse particles with equal (and constant) masses, we have

the following four identities:

$$\begin{aligned} \mathbf{u}_1' + \mathbf{u}_2' &= \mathbf{u}_1 + \mathbf{u}_2 \\ u_1'^2 + u_2'^2 &= e_c^2(u_1^2 + u_2^2) \\ u_1'^2 + u_2'^2 + e_1' + e_2' &= u_1^2 + u_2^2 + e_1 + e_2 \\ e_1' - e_2' &= e_1 - e_2 \end{aligned} \tag{21}$$

corresponding, respectively, to conservation of momentum, kinetic energy, total energy, and equal distribution of change in internal energy. The first three identities come from Newton's laws of motion, while the fourth comes from the assumption that the change in internal energy for each particle is the same, regardless of its velocity or internal energy. It is straightforward to show that $e_1' - e_1 = \frac{1}{2}(1-e_c^2)(u_1^2+u_2^2)$, i.e., the increase in internal energy is proportional to the kinetic energy of the particles before collision. Hence, the change in internal energy of the particle phase e_p is proportional to Θ_p.

Given eq. (21), the collisional source term C on the right-hand side of eq. (8) is modeled using the inelastic BGK closure [5, 44], extended to include internal energy. Using eq. (21), the particle-phase kinetic-energy balance requires $\int \mathbf{u}^2 C\, f \,\mathrm{d}\mathbf{u}\,\mathrm{d}e \leq 0$, and the equality holds for elastic collisions ($e_c = 1$). In general, the inelastic BGK model can be written as [44]

$$C(\mathbf{u}, e) = \frac{\rho_e \alpha_p^\star f_G(\mathbf{u}, e) - f(\mathbf{u}, e)}{\tau_c} \tag{22}$$

where f_G is a Gaussian distribution with the same mean velocity as f (i.e., $\int \mathbf{u} f_G \,\mathrm{d}\mathbf{u}\,\mathrm{d}e = \mathbf{u}_p$) and τ_c is the collision time that depends on α_p and Θ_p:

$$\tau_c = \frac{d_p\sqrt{\pi}}{12\alpha_p g_0 \Theta_p^{1/2}}. \tag{23}$$

For inelastic collisions ($e_c < 1$), the covariance matrix of f_G depends on $\omega = (1 + e_c)/2$ [40], as well as its mean value in e, which is $\int e f_G \,\mathrm{d}\mathbf{u}\,\mathrm{d}e = e_p + (1 - e_c^2)\Theta_p$. In this work, the second-order cross moment in f_G is set to $\int \mathbf{u} e f_G \,\mathrm{d}\mathbf{u}\,\mathrm{d}e = \mathbf{u}_p \int e f_G \,\mathrm{d}\mathbf{u}\,\mathrm{d}e$ (i.e., during a collision $\mathbf{u}$ and e are uncorrelated). However, other choices are possible by changing the fourth identity in eq. (21).

2.2.6. Frictional source term

The frictional source term F is applicable to dense flows with sustained contacts. Physically, the sole purpose of F is to drive the granular temperature Θ_p to a negligible value when $\alpha_p > \alpha_{max}$, thereby producing particle-phase internal energy e_p such that the total energy E_p is conserved. At the same time, all particle velocities are pushed towards $\mathbf{u}_p$, thereby conserving momentum. To satisfy these constraints, the frictional model used in this work is

$$F(\mathbf{u}, e) = \frac{\rho_e \alpha_p^\star \delta(\mathbf{u} - \mathbf{u}_p)\delta(e - e_p - \Theta_p) - f(\mathbf{u}, e)}{\tau_{fr}} \tag{24}$$

where the delta function $\delta(\mathbf{u} - \mathbf{u}_p)$ ensures momentum conservation and $\delta(e - e_p - \Theta_p)$ ensures conservation of E_p. τ_{fr} is a timescale that depends on τ_c and $\partial_{\mathbf{x}} \cdot \mathbf{u}_p$:

$$\tau_{fr} = \frac{c_{fr}}{\max(|\partial_{\mathbf{x}} \cdot \mathbf{u}_p|, 1/\tau_c) h_{fr}}. \tag{25}$$

Here, $c_{fr} = 0.01$ and h_{fr} control the frictional timescale above close packing. The τ_c-dependence makes τ_{fr} very small when $\alpha_p > \alpha_{max}$. The $|\partial_{\mathbf{x}} \cdot \mathbf{u}_p|$-dependence attempts to capture the effect of relative particle motion under such conditions (i.e., in the absence of deformation there is no friction).

2.2.7. Added-mass source term

In the model for added mass, the added mass moving with the particles changes to adapt to the local value of α_p at the rate S_a. This rate does not include possible mass transfer from/to the particles to/from the fluid (e.g., phase change), which is neglected in this work for clarity. Thus, when S_a is positive, fluid is added to the particle wake,

while the opposite occurs when S_a is negative. Such changes will result in changes in the mass, momentum and kinetic energy of each particle in the mesoscale model, which corresponds to the added-mass source term S in eq. (8). At the macroscale, we shall see in section 3 this term yields the expected source terms for mass, momentum and kinetic energy.

At the kinetic level, the added-mass source term is defined by

$$S(\mathbf{u}, e) = C_\xi f + C_u \frac{\partial}{\partial e}[(e - e_f)f] + C_u \frac{\partial}{\partial \mathbf{u}} \cdot [(\mathbf{u} - \mathbf{u}_f)f] + \frac{1}{2} C_u \frac{\partial^2}{\partial \mathbf{u} \partial \mathbf{u}} : (\mathbf{D}_u f). \tag{26}$$

The parameters appearing in this model are

$$C_\xi = \frac{S_a}{\rho_e \alpha_p^\star} = \frac{1}{\tau_a \beta}(\beta^\star - \beta), \quad C_u = \frac{1}{2}(C_\xi + |C_\xi|). \tag{27}$$

Note that $C_u = 0$ when $S_a \leq 0$ (i.e., when added mass is transferred to the fluid phase), otherwise $C_u = C_\xi$. The first term on the right-hand side of eq. (26) represents the change in added mass of a particle (i.e., it generates the source term for the added-mass factor β), the second is transfer of internal energy, the third is acceleration due to change in added mass, and the fourth is the change in fluctuating kinetic energy (proportional to Θ_p) due to the change in added mass. All of these processes occur with constant solid particle mass $\rho_p V_p$, i.e., only the added mass composed of fluid changes. In other words, at the macroscale, the added-mass factor β and $\rho_e \alpha_p^\star$ change when S_a is nonzero, but not $\rho_p \alpha_p$. The model for β in eq. (5) results from this constraint.

The velocity diffusion matrix in eq. (26) is defined by

$$\mathbf{D}_u = (\mathbf{u} - \mathbf{u}_f) \otimes (\mathbf{u} - \mathbf{u}_f) + \frac{2}{3} k_f \mathbf{I} \tag{28}$$

where $\mathbf{u}_f$ is the fluid-phase velocity and k_f is the PTKE. The final term in eq. (28) represents an isotropic model for the PTKE Reynolds-stress tensor. Thus, if the PTKE model is extended to include the full Reynolds-stress tensor, it should be used in place of the isotropic model. Physically, this diffusion term represents the random acceleration of a particle due to the addition (i.e., $C_\xi > 0$) of fluid-phase PTKE as well as to the velocity difference $|\mathbf{u} - \mathbf{u}_f|$.

2.3. Range of validity of mesoscale model

Compared to the full kinetic-theory expression for inelastic hard-sphere collisions [40], the main simplification in eq. (8) is the treatment of collisional pressure. In the full model for hard spheres, the collisional pressure depends on a complicated integral with respect to the two-particle velocity distribution function [18]. Moreover, the collisions generate a viscous stress tensor that can be derived from the KTGF, and which will be important for low-speed, moderately dense cases with mean shear. Such terms are most easily implemented in the macroscale momentum balance and depend on gradients of $\mathbf{u}_p$.

In terms of the volume fraction, the kinetic model in eq. (8) is valid for all physically possible values of α_p, including $\alpha_p \to 0$. Note, however, that for very dilute flows particle–particle collisions are negligible so that the terms P_p, C and F can be dropped in eq. (8). The kinetic model can then be approximated by a Lagrangian method that follows each individual particle. In the next section, we develop a macroscale model for $\alpha_p > 0.001$, i.e., particle flows wherein collisions cannot be neglected. While such models can, in principle, be employed for more dilute flows, the closures used for the free-transport terms are challenging [20] because the shape of the VDF is often far from Gaussian, and the spatial flux of the particles is strongly dependent on the shape of the VDF. In cases without collisions and/or strong fluid drag, Lagrangian methods for solving eq. (8) (which do not assume a form for the VDF) will usually be more accurate than the macroscale model presented below.

3. Macroscale model for the particle phase

Hereinafter, the dependence of functions on $(t, \mathbf{x})$ is dropped, and the following notation is used to denote the moments of the MDF:

$$\langle \varphi \rangle = \int \varphi(\mathbf{u}, e) f(\mathbf{u}, e) \, \mathrm{d}\mathbf{u} \, \mathrm{d}e \tag{29}$$

for any function φ. To account for the added mass, the NDF is multiplied the particle mass $m_p^\star$ such that the conserved particle-phase variables (i.e., mass, momentum, internal energy, kinetic energy) are defined, respectively, by

$$\langle 1 \rangle = \rho_e \alpha_p^\star, \quad \langle \mathbf{u} \rangle = \rho_e \alpha_p^\star \mathbf{u}_p, \quad \langle \frac{1}{2}\mathbf{u}^2 \rangle = \rho_e \alpha_p^\star K_p, \quad \langle e \rangle = \rho_e \alpha_p^\star e_p. \tag{30}$$

For the macroscale model, we will close the moment equations found from the kinetic model in the previous section at the level of the particle-phase kinetic energy (i.e., a Maxwellian velocity distribution function), which is sufficient for describing high-speed collisional and/or low-Stokes-number flows. Nevertheless, the kinetic model can also be used to find transport equations for higher-order moments, such as for the anisotropic Gaussian model [32, 53] or quadrature-based moment methods [21], that are needed for weakly collisional or collision-less flows.

In the following, we first consider in section 3.1 the source terms due to added mass that are needed in the macroscale models. We then move to the velocity moments in section 3.2 and their governing equations in section 3.3, before turning to the moments involving the internal energy in section 3.4. Finally, the closures used for the macroscale model are discussed in section 3.5, and the closed transport equations for the particle phase are given in section 3.6.

3.1. Added-mass source terms in macroscale model

The added-mass source terms in the macroscale model for the moments in eq. (30) appear in closed form. They are found by integration over phase space, i.e.,

$$\int S(\mathbf{u}, e)\, \mathrm{d}\mathbf{u}\, \mathrm{d}e = S_a, \quad \int \mathbf{u} S(\mathbf{u}, e)\, \mathrm{d}\mathbf{u}\, \mathrm{d}e = \mathbf{S}_{gp}, \quad \int \frac{1}{2} u^2 S(\mathbf{u}, e)\, \mathrm{d}\mathbf{u}\, \mathrm{d}e = S_K, \quad \int e\, S(\mathbf{u}, e)\, \mathrm{d}\mathbf{u}\, \mathrm{d}e = S_e. \tag{31}$$

Using eq. (26) to define $S(\mathbf{u}, e)$, the added-mass source terms for the moments are found by evaluating these integrals. This procedure yields

$$\mathbf{S}_{gp} = \max(S_a, 0)\, \mathbf{u}_f + \min(S_a, 0)\, \mathbf{u}_p, \tag{32}$$

$$S_K = \max(S_a, 0)\, K_f + \min(S_a, 0)\, K_p, \tag{33}$$

and

$$S_e = \max(S_a, 0)\, e_f + \min(S_a, 0)\, e_p. \tag{34}$$

As shown below, these source terms ensure conservation of mass, internal energy, momentum, and kinetic energy for the sum of the two phases. Indeed, for the total-energy source term needed for the fluid phase, we find

$$S_E = \max(S_a, 0)\, E_f + \min(S_a, 0)\, E_p, \tag{35}$$

such that $S_E = S_K + S_e$ as expected. In any case, using eq. (26) the added-mass source terms for moments of the MDF of any order will appear in closed form.

3.2. Velocity moments

We first derive the unclosed governing equation for the velocity moments with integer order, before introducing the closures found by assuming the velocity distribution function (VDF) is Maxwellian in section 3.5. The velocity moment of integer order $l = i + j + k$ is defined by[3]

$$M^l_{i,j,k} = \int u^i v^j w^k f(\mathbf{u}, e)\ \mathrm{d}\mathbf{u}\, \mathrm{d}e = \int u^i v^j w^k f(\mathbf{u})\ \mathrm{d}\mathbf{u} = \langle u^i v^j w^k \rangle \tag{36}$$

where the vector $\mathbf{u} = (u, v, w)^t$ corresponds to the velocity components in directions $\mathbf{x} = (x, y, z)^t$, and $f(\mathbf{u})$ is the mass-weighted VDF. The lower-order moments of the VDF have a physical interpretation. For example, the zero-order moment

$$M^0 = \rho_e \alpha_p^\star \tag{37}$$

[3]The velocity moments can also be defined using a vector/tensor notation. For example, the vector of first-order moments is $\mathbf{M}^1 = \langle \mathbf{u} \rangle$, and the second-order tensor is $\mathbf{M}^2 = \langle \mathbf{u} \otimes \mathbf{u} \rangle$. Higher-order moments are defined similarly using direct products of $\mathbf{u}$. Such notation is particularly useful when working with non-Cartesian coordinates, and when decomposing the velocity into its mean and fluctuating components.

is the mass of the particle phase (including added mass), and the vector of first-order moments

$$\mathbf{M}^1 = (M_{1,0,0}, M_{0,1,0}, M_{0,0,1})^t = \rho_e \alpha_p^\star \mathbf{u}_p \tag{38}$$

with mean velocity $\mathbf{u}_p = (u_p, v_p, w_p)^t$ is its momentum. The non-negative, symmetric, second-order tensor $\mathbf{M}^2$ can be written in terms of its components:

$$\mathbf{M}^2 = \begin{pmatrix} M_{2,0,0} & M_{1,1,0} & M_{1,0,1} \\ M_{1,1,0} & M_{0,2,0} & M_{0,1,1} \\ M_{1,0,1} & M_{0,1,1} & M_{0,0,2} \end{pmatrix}, \tag{39}$$

and can be further decomposed as $\mathbf{M}^2 = \rho_e \alpha_p^\star (\mathbf{u}_p \otimes \mathbf{u}_p + \boldsymbol{\sigma})$ where $\boldsymbol{\sigma}$ is the non-negative velocity covariance matrix. A full second-order moment closure would solve the ten transport equations for the independent moments in eqs. (37) to (39) [53]. In this work, the macroscale model solves for the trace of $\mathbf{M}^2$, denoted by M^2.

3.3. Transport equation for velocity moments

The kinetic model in eq. (8) yields an unclosed transport equation for the particle-phase velocity moments. In Cartesian coordinates, we find for $i, j, k \geq 0$ and $l = i + j + k$ (moments with negative subscripts i, j, k are null):

$$\begin{aligned}
\partial_t M^l_{i,j,k} + \partial_x(M^{l+1}_{i+1,j,k} + iP_p M^{l-1}_{i-1,j,k}) + \partial_y(M^{l+1}_{i,j+1,k} + jP_p M^{l-1}_{i,j-1,k}) + \partial_z(M^{l+1}_{i,j,k+1} + kP_p M^{l-1}_{i,j,k-1}) = \\
i\langle u^{i-1}v^j w^k A_{u,x}\rangle + j\langle u^i v^{j-1} w^k A_{u,y}\rangle + k\langle u^i v^j w^{k-1} A_{u,z}\rangle \\
+ i(i-1)\langle u^{i-2}v^j w^k B_{u,xx}\rangle + j(j-1)\langle u^i v^{j-2} w^k B_{u,yy}\rangle + k(k-1)\langle u^i v^j w^{k-2} B_{u,zz}\rangle \\
+ 2ij\langle u^{i-1}v^{j-1} w^k B_{u,xy}\rangle + 2ik\langle u^i v^j w^{k-1} B_{u,xz}\rangle + 2jk\langle u^i v^{j-1} w^{k-1} B_{u,zz}\rangle \\
- \frac{i}{\rho_e}(\partial_x \hat{p}_f + F_{pf,x}) M^{l-1}_{i-1,j,k} - \frac{j}{\rho_e}(\partial_y \hat{p}_f + F_{pf,y}) M^{l-1}_{i,j-1,k} - \frac{k}{\rho_e}(\partial_z \hat{p}_f + F_{pf,z}) M^{l-1}_{i,j,k-1} \\
- i\frac{M^{l-1}_{i-1,j,k}}{\rho_e \alpha_p^\star}(\partial_{\mathbf{x}} \cdot \mathbf{P}_{pfp})_x - j\frac{M^{l-1}_{i,j-1,k}}{\rho_e \alpha_p^\star}(\partial_{\mathbf{x}} \cdot \mathbf{P}_{pfp})_y - k\frac{M^{l-1}_{i,j,k-1}}{\rho_e \alpha_p^\star}(\partial_{\mathbf{x}} \cdot \mathbf{P}_{pfp})_z + C_{i,j,k} + F_{i,j,k} + S_{i,j,k}.
\end{aligned} \tag{40}$$

Here, the pressure terms involving P_p, the force terms for buoyancy and $\mathbf{F}_{pf}$, and the pfp-pressure terms are in closed form; hence, they need no further discussion. The other terms in eq. (40) can be expanded out as shown below. However, it must be emphasized that, except for the free-transport term, all of the other terms in eq. (40) are in closed form given all moments up to order l. This is a result of the choices made when formulating the mesoscale model (e.g., τ_p does not depend on $\mathbf{u}$, etc.). If nonlinear models were used, other unclosed terms would arise and would be closed using, for example, quadrature-based moment methods [40].

3.3.1. Free-transport term for velocity moments

Because it requires the moments of order $l + 1$, the only unclosed term in eq. (40) is the free-transport spatial flux, e.g., $M^{l+1}_{i+1,j,k}$. In general, if we keep moments up to $\mathbf{M}^2$, the macroscale model requires a closure for the third-order moments $\mathbf{M}^3$. The closure used for the macroscale model is discussed in section 3.5. However, we should reemphasize that the macroscale model can be extended to more dilute regimes by including higher-order velocity moments, e.g., $\mathbf{M}^4$ as done in [20] by closing $\mathbf{M}^5$. The validity of the resulting macroscale model can then be tested against Euler–Lagrange solutions for the mesoscale model.

3.3.2. Acceleration terms for velocity moments

The fluid-drag source terms found from the mesoscale model are

$$\begin{aligned}
\langle u^{i-1}v^j w^k A_{u,x}\rangle &= \frac{1}{\tau_p}(u_f M^{l-1}_{i-1,j,k} - M^l_{i,j,k}) \\
\langle u^i v^{j-1} w^k A_{u,y}\rangle &= \frac{1}{\tau_p}(v_f M^{l-1}_{i,j-1,k} - M^l_{i,j,k}) \\
\langle u^i v^j w^{k-1} A_{u,z}\rangle &= \frac{1}{\tau_p}(w_f M^{l-1}_{i,j,k-1} - M^l_{i,j,k})
\end{aligned} \tag{41}$$

with fluid velocity components (u_f, v_f, w_f). The six independent diffusion terms are

$$\begin{aligned}
\langle u^{i-2}v^j w^k B_{u,xx}\rangle &= \frac{1-a}{\tau_p}\left[M^l_{i,j,k} - 2u_p M^{l-1}_{i-1,j,k} + \left(u_p^2 + \frac{2}{3}k_f\right)M^{l-2}_{i-2,j,k}\right] \\
\langle u^i v^{j-2} w^k B_{u,yy}\rangle &= \frac{1-a}{\tau_p}\left[M^l_{i,j,k} - 2v_p M^{l-1}_{i,j-1,k} + \left(v_p^2 + \frac{2}{3}k_f\right)M^{l-2}_{i,j-2,k}\right] \\
\langle u^i v^j w^{k-2} B_{u,zz}\rangle &= \frac{1-a}{\tau_p}\left[M^l_{i,j,k} - 2w_p M^{l-1}_{i,j,k-1} + \left(w_p^2 + \frac{2}{3}k_f\right)M^{l-2}_{i,j,k-2}\right] \\
\langle u^{i-1}v^{j-1} w^k B_{u,xy}\rangle &= \frac{1-a}{\tau_p}(M^l_{i,j,k} - u_p M^{l-1}_{i-1,j,k} - v_p M^{l-1}_{i,j-1,k} + u_p v_p M^{l-2}_{i-1,j-1,k}) \\
\langle u^{i-1}v^j w^{k-1} B_{u,xz}\rangle &= \frac{1-a}{\tau_p}(M^l_{i,j,k} - u_p M^{l-1}_{i-1,j,k} - w_p M^{l-1}_{i,j,k-1} + u_p w_p M^{l-2}_{i-1,j,k-1}) \\
\langle u^i v^{j-1} w^{k-1} B_{u,yz}\rangle &= \frac{1-a}{\tau_p}(M^l_{i,j,k} - v_p M^{l-1}_{i,j-1,k} - w_p M^{l-1}_{i,j,k-1} + v_p w_p M^{l-2}_{i,j-1,k-1})
\end{aligned} \tag{42}$$

and the other three components are found using symmetry. As noted earlier, the acceleration terms are closed for any order of the velocity moments.

3.3.3. Collisional and frictional terms for velocity moments

In the macroscale model, the source terms $C_{i,j,k}$ and $F_{i,j,k}$ up to second order are closed given the three moments M^0, $\mathbf{M}^1$ and $\mathbf{M}^2$. In general, the inelastic BGK model for collisions introduced in section 2.2.5 yields

$$C_{i,j,k} = \frac{1}{\tau_c}(\rho_e \alpha_p^\star G_{i,j,k} - M^l_{i,j,k}) \tag{43}$$

where $G_{i,j,k}$ is the moment from the Gaussian distribution f_G. Similarly, the frictional model yields

$$F_{i,j,k} = \frac{1}{\tau_f}(\rho_e \alpha_p^\star u_p^i v_p^j w_p^k - M^l_{i,j,k}). \tag{44}$$

Due to conservation of mass and momentum, $C_{0,0,0} = C_{1,0,0} = C_{0,1,0} = C_{0,0,1} = 0$ and $F_{0,0,0} = F_{1,0,0} = F_{0,1,0} = F_{0,0,1} = 0$. In any case, these terms are closed given all moments up to $M^l_{i,j,k}$ for any $l \geq 0$.

3.3.4. Added-mass terms for velocity moments

Given the moments $M^l_{i,j,k}$, the added-mass source term with the coefficients C_ξ and C_u given by eq. (27) is

$$\begin{aligned}
S_{i,j,k} &= C_\xi M^l_{i,j,k} + i\,C_u(u_f M^{l-1}_{i-1,j,k} - M^l_{i,j,k}) + j\,C_u(v_f M^{l-1}_{i,j-1,k} - M^l_{i,j,k}) + k\,C_u(w_f M^{l-1}_{i,j,k-1} - M^l_{i,j,k}) \\
&+ i(i-1)\frac{1}{2}C_u\left[M^l_{i,j,k} - 2u_f M^{l-1}_{i-1,j,k} + \left(u_f^2 + \frac{2}{3}k_f\right)M^{l-2}_{i-2,j,k}\right] + j(j-1)\frac{1}{2}C_u\left[M^l_{i,j,k} - 2v_f M^{l-1}_{i,j-1,k} + \left(v_f^2 + \frac{2}{3}k_f\right)M^{l-2}_{i,j-2,k}\right] \\
&\qquad + k(k-1)\frac{1}{2}C_u\left[M^l_{i,j,k} - 2w_f M^{l-1}_{i,j,k-1} + \left(w_f^2 + \frac{2}{3}k_f\right)M^{l-2}_{i,j,k-2}\right] \\
&+ ij\,C_u(M^l_{i,j,k} - u_f M^{l-1}_{i-1,j,k} - v_f M^{l-1}_{i-1,j,k} + u_f v_f M^{l-2}_{i-1,j-1,k}) + ik\,C_u(M^l_{i,j,k} - u_f M^{l-1}_{i,j,k-1} - w_f M^{l-1}_{i-1,j,k} + u_f w_f M^{l-2}_{i-1,j,k-1}) \\
&\qquad + jk\,C_u(M^l_{i,j,k} - v_f M^{l-1}_{i,j,k-1} - w_f M^{l-1}_{i,j-1,k} + v_f w_f M^{l-2}_{i,j-1,k-1}).
\end{aligned} \tag{45}$$

Although it appears complicated, this expression is in closed form for all choices of (i, j, k). For the macroscale model used in this work, we will need source terms for seven moments up to second order:

$$(i, j, k) \in \{(0,0,0), (1,0,0), (0,1,0), (0,0,1), (2,0,0) + (0,2,0) + (0,0,2)\},$$

i.e., for the moments given in eq. (30). Thus, all of the covariance components from eq. (45) will drop out in the kinetic energy balance.

3.4. Internal-energy moments

For the macroscale model, only two moments involving internal energy are needed for closure: e_p and its spatial flux $\langle e\mathbf{u}\rangle$. Consistent with [28], for high-speed flows we use the closure $\langle e\mathbf{u}\rangle = \rho_e \alpha_p^\star e_p \mathbf{u}_p$; however, including a term for conduction in low-speed granular flows is also possible using the KTGF [4, 30]. The mesoscale model in eq. (8) yields the balance equation for particle-phase internal energy:

$$\partial_t \rho_e \alpha_p^\star e_p + \partial_{\mathbf{x}} \cdot \rho_e \alpha_p^\star e_p \mathbf{u}_p = H_p - H_{pf} + S_e \tag{46}$$

where the heat-transfer term is

$$H_{pf} = -\langle A_e \rangle = \frac{6\alpha_p^\star \lambda_f Nu}{d_p^2}(T_p - T_f), \tag{47}$$

which is in closed form. The term H_p is equal to $\int e(C + F)\,\mathrm{d}\mathbf{u}\,\mathrm{d}e$, and S_e (see eq. (34)) is due to added mass.

The collisional and frictional terms, $\int eC\,\mathrm{d}\mathbf{u}\,\mathrm{d}e$ and $\int eF\,\mathrm{d}\mathbf{u}\,\mathrm{d}e$, are strictly non-negative [28]. The frictional contribution due to the transfer of particle-phase kinetic energy to internal energy is

$$\int eF\,\mathrm{d}\mathbf{u}\,\mathrm{d}e = -\,\partial_t \rho_e \alpha_p^\star K_p\big|_{fr} = \rho_e \alpha_p^\star \frac{1}{\tau_{fr}}\Theta_p, \tag{48}$$

which drives Θ_p quickly to zero above close packing. The collisional contribution to the particle-phase heating term is

$$\int eC\,\mathrm{d}\mathbf{u}\,\mathrm{d}e = -\,\partial_t \rho_e \alpha_p^\star K_p\big|_{c} = \rho_e \alpha_p^\star \frac{(1 - e_c^2)}{\tau_c}\Theta_p. \tag{49}$$

The particle-phase heating rate in eq. (46) is thus

$$H_p = \rho_e \alpha_p^\star \left[\frac{1}{\tau_c}(1 - e_c^2) + \frac{1}{\tau_{fr}}\right]\Theta_p \tag{50}$$

where the collision time τ_c is defined in eq. (23) and the frictional time scale τ_{fr} is defined in eq. (25). Although they are not needed in this work, the identities in eq. (21) also fix $\int e^2 C\,\mathrm{d}\mathbf{u}\,\mathrm{d}e$ and $\int e\mathbf{u}C\,\mathrm{d}\mathbf{u}\,\mathrm{d}e$, and hence the corresponding terms in the covariance matrix of f_G are in closed form for any choice of moments used to define the macroscale model.

3.5. Closures for velocity moments used in the macroscale model

In the macroscale model, we use an isotropic second-order moment closure where $\boldsymbol{\sigma}$ is replaced by $\frac{1}{3}tr(\boldsymbol{\sigma})\mathbf{I} = \Theta_p \mathbf{I}$, which corresponds to a Maxwellian distribution. The particle-phase kinetic energy will then be a scalar:

$$M^2 = tr(\mathbf{M}^2) = M_{2,0,0} + M_{0,2,0} + M_{0,0,2} = \rho_e \alpha_p^\star (u_p^2 + 3\Theta_p) \quad \Longrightarrow \quad M^2 = 2\rho_e \alpha_p^\star K_p. \tag{51}$$

This level of closure corresponds to the Euler equation for the particle phase. The central velocity moments, defined by

$$C^l_{i,j,k} = \frac{1}{M^0}\int (u - u_p)^i (v - v_p)^j (w - w_p)^k f\,(\mathbf{u})\,\mathrm{d}\mathbf{u}, \tag{52}$$

are thus null when l is odd. As shown next, this fact is used to close the spatial flux of M^2, which depends on third-order moments.

Assuming that the VDF is Maxwellian, the closure for the third-order velocity moments is

$$\begin{aligned}
M^3_{3,0,0} &= M^0(3u_pC^2_{2,0,0} + u_p^3) = \rho_e\alpha_p^\star(3\Theta_p + u_p^2)u_p \\
M^3_{2,1,0} &= M^0(v_pC^2_{2,0,0} + 2u_pC^2_{1,1,0} + u_p^2v_p) = \rho_e\alpha_p^\star(\Theta_p + u_p^2)v_p \\
M^3_{2,0,1} &= M^0(w_pC^2_{2,0,0} + 2u_pC^2_{1,0,1} + u_p^2w_p) = \rho_e\alpha_p^\star(\Theta_p + u_p^2)w_p \\
M^3_{1,1,1} &= M^0(u_pC^2_{0,1,1} + v_pC^2_{1,0,1} + w_pC^2_{1,1,0} + u_pv_pw_p) = \rho_e\alpha_p^\star u_pv_pw_p
\end{aligned} \tag{53}$$

and the other third-order moments are found by permuting the indices. In these closures, the second-order central moments are treated as isotropic:

$$C^2_{i,j,k} = \Theta_p(\delta_{i,2} + \delta_{j,2} + \delta_{k,2}) \quad \Longrightarrow \quad \mathbf{C}^2 = \Theta_p\mathbf{I}. \tag{54}$$

The components of the spatial flux for M^2 are then

$$\begin{aligned}
F^2_x &= M^3_{3,0,0} + M^3_{1,2,0} + M^3_{1,0,2} = \rho_e\alpha_p^\star(5\Theta_p + u_p^2 + v_p^2 + w_p^2)u_p \\
F^2_y &= M^3_{2,1,0} + M^3_{0,3,0} + M^3_{0,1,2} = \rho_e\alpha_p^\star(5\Theta_p + u_p^2 + v_p^2 + w_p^2)v_p \\
F^2_z &= M^3_{2,0,1} + M^3_{0,2,1} + M^3_{0,0,3} = \rho_e\alpha_p^\star(5\Theta_p + u_p^2 + v_p^2 + w_p^2)w_p
\end{aligned} \tag{55}$$

i.e., the flux vector for kinetic energy is $\mathbf{F}^2 = 2\rho_e\alpha_p^\star(K_p + \Theta_p)\mathbf{u}_p = M^2\mathbf{u}_p + 2\rho_e\alpha_p^\star\Theta_p\mathbf{u}_p$. Using, for example, extended kinetic theory [4], the momentum flux could be extended to viscous granular flows by adding the appropriate closures. For the high-speed flows, such terms are very small compared to the granular pressure terms.

Given the results in eqs. (41) and (42), the fluid-drag contribution to the particle-phase kinetic energy K_p is

$$D_E = \frac{1}{\tau_p}[M^2 - \rho_e\alpha_p^\star\mathbf{u}_f\cdot\mathbf{u}_p - (1-a)(\langle B_{u,xx}\rangle + \langle B_{u,yy}\rangle + \langle B_{u,zz}\rangle)] = \frac{\rho_e\alpha_p^\star}{\tau_p}[3a\Theta_p - 2(1-a)k_f + \mathbf{u}_{pf}\cdot\mathbf{u}_p] \tag{56}$$

where M^2 has been replaced with the isotropic closure for the velocity covariance. This term represents kinetic-energy transfer to the fluid from particles ($D_E > 0$) or vice versa ($D_E < 0$).

3.6. Transport equations used in the macroscale model

For the particle phase, the macroscale model involves six transport equations. The first four equations are for mass and momentum:

$$\partial_tM^0_{0,0,0} + \partial_xM^1_{1,0,0} + \partial_yM^1_{0,1,0} + \partial_zM^1_{0,0,1} = S_a \tag{57}$$

$$\begin{aligned}
&\partial_tM^1_{1,0,0} + \partial_x(M^2_{2,0,0} + P_pM^0_{0,0,0}) + \partial_yM^2_{1,1,0} + \partial_zM^2_{1,0,1} = \langle A_{u,x}\rangle - \alpha_p^\star(\partial_x\hat{p}_f + F_{pf,x}) - (\partial_\mathbf{x}\cdot\mathbf{P}_{pfp})_x + (\mathbf{S}_{gp})_x \\
&\partial_tM^1_{0,1,0} + \partial_xM^2_{1,1,0} + \partial_y(M^2_{0,2,0} + P_pM^0_{0,0,0}) + \partial_zM^2_{0,1,1} = \langle A_{u,y}\rangle - \alpha_p^\star(\partial_y\hat{p}_f + F_{pf,y}) - (\partial_\mathbf{x}\cdot\mathbf{P}_{pfp})_y + (\mathbf{S}_{gp})_y \\
&\partial_tM^1_{0,0,1} + \partial_xM^2_{1,0,1} + \partial_yM^2_{0,1,1} + \partial_z(M^2_{0,0,2} + P_pM^0_{0,0,0}) = \langle A_{u,z}\rangle - \alpha_p^\star(\partial_z\hat{p}_f + F_{pf,z}) - (\partial_\mathbf{x}\cdot\mathbf{P}_{pfp})_z + (\mathbf{S}_{gp})_z
\end{aligned} \tag{58}$$

The fifth equation is for the scalar M^2:

$$\partial_tM^2 + \partial_\mathbf{x}\cdot[(M^2 + 2\rho_e\alpha_p^\star\Theta_p + 2\rho_e\alpha_p^\star P_p)\mathbf{u}_p] = -2D_E - 2\alpha_p^\star\mathbf{u}_p\cdot(\partial_\mathbf{x}\hat{p}_f + \mathbf{F}_{pf}) - 2\mathbf{u}_p\cdot(\partial_\mathbf{x}\cdot\mathbf{P}_{pfp}) - 2H_p + 2S_K, \tag{59}$$

and the sixth equation is eq. (46) for the internal energy e_p. The kinetic-pressure tensor in eq. (58) can be rewritten in tensor notation:

$$\begin{bmatrix} M^2_{2,0,0} & M^2_{1,1,0} & M^2_{1,0,1} \\ M^2_{1,1,0} & M^2_{0,2,0} & M^2_{0,1,1} \\ M^2_{1,0,1} & M^2_{0,1,1} & M^2_{0,0,2} \end{bmatrix} = M^0_{0,0,0}(\mathbf{u}_p\otimes\mathbf{u}_p + \Theta_p\mathbf{I}). \tag{60}$$

The trace of this tensor is $M^2 = M_{2,0,0} + M_{0,2,0} + M_{0,0,2} = 2M^0_{0,0,0}K_p$. In eq. (59), H_p is particle-phase kinetic-to-internal-energy transfer due to inelastic collisions and friction (see eq. (50)). Note that it has the opposite sign in the particle-phase internal energy balance.

4. Final form of the macroscale model

The principal objective of this section is to review how added mass, internal energy, and PKTE are treated for the fluid phase based on the hyperbolic two-fluid model from [18, 22]. The mass, momentum and kinetic-energy exchange terms have been found for the particle phase from the mesoscale model. The same terms will appear in the fluid-phase equation with the opposite sign.

4.1. Macroscale model for fluid phase

In conservative form, the continuous fluid phase is governed by mass, momentum, total-energy, and PTKE balances (neglecting gravity for simplicity) [22]:

$$\partial_t \rho_f \alpha_f^\star + \partial_{\mathbf{x}} \cdot \rho_f \alpha_f^\star \mathbf{u}_f = -S_a \tag{61}$$

$$\partial_t \rho_f \alpha_f^\star \mathbf{u}_f + \partial_{\mathbf{x}} \cdot (\rho_f \alpha_f^\star \mathbf{u}_f \otimes \mathbf{u}_f + \hat{p}_f \mathbf{I}) = \alpha_p^\star (\partial_{\mathbf{x}} \hat{p}_f + \mathbf{F}_{pf}) + \mathbf{D} - \mathbf{S}_{gp} \tag{62}$$

$$\partial_t \rho_f \alpha_f^\star E_f + \partial_{\mathbf{x}} \cdot [\rho_f \alpha_f^\star \mathbf{u}_f E_f + (\alpha_f^\star \mathbf{u}_f + \alpha_p^\star \mathbf{u}_p)\hat{p}_f] = -\mathbf{P}_{pfp} : (\partial_{\mathbf{x}} \mathbf{u}_p) + \alpha_p^\star \mathbf{u}_p \cdot (\partial_{\mathbf{x}} \hat{p}_f + \mathbf{F}_{pf}) + D_E + H_{pf} - S_E \tag{63}$$

$$\partial_t \rho_f \alpha_f^\star k_f + \partial_{\mathbf{x}} \cdot \rho_f \alpha_f^\star \mathbf{u}_f k_f + \frac{2}{3} \rho_f \alpha_f^\star k_f \partial_{\mathbf{x}} \cdot \mathbf{u}_f = D_{PT} - \rho_e \alpha_p^\star \frac{C_f}{\tau_p} k_f. \tag{64}$$

Notice that the total energy flux contains the term $(\alpha_f^\star \mathbf{u}_f + \alpha_p^\star \mathbf{u}_p)\hat{p}_f$ where $(\alpha_f^\star \mathbf{u}_f + \alpha_p^\star \mathbf{u}_p)$ is the volume-average mixture velocity. This term is exact and arises due to the excluded volume occupied by the particles [18]. Physically, it changes the speed of sound in the fluid phase when particles are present. Also notice that the pfp-pressure tensor appears in the total energy equation as a work term, i.e., the fluid does work on the particles to lower α_p.

The fluid pressure is found from an equation of state. In this work, we will use the stiffened-gas law:

$$p_f = (\gamma_f - 1)\rho_f \left(E_f - K_f\right) - \gamma_f p_{\infty,f} = (\gamma_f - 1)\rho_f e_f - \gamma_f p_{\infty,f} \tag{65}$$

where γ_f is the heat-capacity ratio. For an ideal gas, the reference pressure $p_{\infty,f}$ is set to 0, leading to the well-known ideal-gas law. In liquids, $p_{\infty,f} > 0$ is used to control the speed of sound.

The terms $\mathbf{D}$ and D_{PT} represent drag exchange:

$$\mathbf{D} = \frac{\rho_e \alpha_p^\star}{\tau_p} \mathbf{u}_{pf}, \quad D_{PT} = \frac{\rho_e \alpha_p^\star}{\tau_p} [u_{pf}^2 + 3a\Theta_p - 2(1-a)k_f]. \tag{66}$$

Physically, $D_{PT} \geq 0$ represents kinetic energy lost from the particle phase to produce PTKE in the fluid phase. This kinetic energy comes from both the mean (u_p^2) and fluctuating (Θ_p) components.

The parameter C_f in eq. (64) controls the rate of dissipation of PTKE into internal energy in the fluid phase [49]. Here, we will use the correlation from PR-DNS with frozen particles [42]:

$$C_f^{-1} = \alpha_p [1 + 1.25\alpha_f^3 \exp(-\alpha_p \alpha_f^{1/2} Re_p^{1/2})]. \tag{67}$$

At a steady state with constant u_{pf}, we then find

$$\frac{k_f}{u_{pf}^2} \to C_f^{-1}, \quad \Theta_p \to \frac{2(1-a)}{3a} k_f. \tag{68}$$

The correlation in eq. (67) is valid for uniform α_p. When k_f is transported from a uniform region to a very dilute region (e.g., behind a particle curtain), C_f from eq. (67) can be much too large. Possible alternatives are to replace, in dilute regions, C_f/τ_p by $C_f^* k_f^{1/2}/d_p$ where C_f^* is a constant of order one, or to solve a transport equation for pseudoturbulence frequency ω_{pt} [19, 49].

4.2. Macroscale model for particle phase

The mass balance in eq. (57) can be rewritten in a more familiar form using tensor notation:

$$\partial_t \rho_e \alpha_p^\star + \partial_{\mathbf{x}} \cdot \rho_e \alpha_p^\star \mathbf{u}_p = S_a. \tag{69}$$

Likewise, the momentum balance in eq. (58) can be rewritten as

$$\partial_t \rho_e \alpha_p^\star \mathbf{u}_p + \partial_{\mathbf{x}} \cdot [\rho_e \alpha_p^\star (\mathbf{u}_p \otimes \mathbf{u}_p + \Theta_p \mathbf{I} + P_p \mathbf{I}) + \mathbf{P}_{pfp}] = -\alpha_p^\star (\partial_{\mathbf{x}} \hat{p}_f + \mathbf{F}_{pf}) - \mathbf{D} + \mathbf{S}_{gp}. \tag{70}$$

The kinetic-energy balance in eq. (59) can be rewritten as

$$\partial_t \rho_e \alpha_p^\star K_p + \partial_{\mathbf{x}} \cdot [\rho_e \alpha_p^\star (K_p + \Theta_p + P_p)\mathbf{u}_p + \mathbf{P}_{pfp} \cdot \mathbf{u}_p] = \mathbf{P}_{pfp} : (\partial_{\mathbf{x}} \mathbf{u}_p) - \alpha_p^\star \mathbf{u}_p \cdot (\partial_{\mathbf{x}} \hat{p}_f + \mathbf{F}_{pf}) - D_E - H_p + S_K, \tag{71}$$

and the internal energy is found from eq. (46). From the momentum and kinetic-energy balances, it can be shown that the pfp-pressure tensor does not change Θ_p.

If needed, the balance equation for the total energy $E_p = K_p + e_p$ can be found by summing eqs. (46) and (71). Comparing the total-energy balances, it can be easily seen that the sum of the total energies of the two phases is conserved. The same is true for the mass and momentum balances. In absence of the frictional pressure, the mathematical properties of macroscale model have been investigated in [22] where it is shown that the model is well-posed. Note that when the frictional pressure is present ($\alpha_p > \alpha_{max}$), it will determine the speed of sound in the particle phase, independent of the fluid phase. Finally, as noted earlier, the macroscale model is completed by solving for either β or $\rho_p \alpha_p$. For convenience, hereinafter we solve the balance equation for the latter.

4.3. Determination of primitive variables from the conserved variables

To conclude the definition of the macroscale model, note that given α_p and the two conserved variables for the phase masses (i.e., $\rho_e \alpha_p^\star$ and $\rho_f \alpha_f^\star$), α_a is found from

$$\alpha_a = \frac{\kappa}{1+\kappa} \alpha_f \qquad \text{for} \qquad \kappa = \frac{\rho_e \alpha_p^\star - \rho_p \alpha_p}{\rho_f \alpha_f^\star} = \frac{\alpha_a}{\alpha_f^\star} \tag{72}$$

with $\alpha_f = 1 - \alpha_p$, and then $\alpha_p^\star = \alpha_p + \alpha_a$ and $\alpha_f^\star = \alpha_f - \alpha_a$. Finally, ρ_f is found from $\rho_f \alpha_f^\star$. Thus, for constant ρ_p, the independent primitive variables (α_p, $\alpha_p^\star$, ρ_f, $\mathbf{u}_p$, $\mathbf{u}_f$, K_p, e_p, E_f, k_f) are uniquely defined from the conserved variables ($\rho_p \alpha_p$, $\rho_e \alpha_p^\star$, $\rho_f \alpha_f^\star$, $\rho_e \alpha_p^\star \mathbf{u}_p$, $\rho_f \alpha_f^\star \mathbf{u}_f$, $\rho_e \alpha_p^\star K_p$, $\rho_e \alpha_p^\star e_p$, $\rho_f \alpha_f^\star E_f$, $\rho_f \alpha_f^\star k_f$), and ρ_e is found from eq. (4). Likewise, the dependent primitive variables (α_f, $\alpha_f^\star$) are found from the constraints $\alpha_p + \alpha_f = 1$ and $\alpha_p^\star + \alpha_f^\star = 1$.

The nine-equation macroscale model for fluid–particle flow with added mass, internal energy, and PTKE is summarized in table 1 with parameters defined in table 2. Example values for the model constants in gas–particle flows are given in table 3. However, for specific fluid and solid phases, the thermodynamic properties must be specified for each application. For example, it may be necessary to account for the temperature dependence of the heat capacities when defining the internal energies, and the fluid-phase viscosity. For the shock–particle-curtain cases, the definition of the drag coefficient C_D may need to depend on the Mach number [6].

5. Numerical implementation of macroscale model

In this section, the solution procedure for the coupled fluid–particle system of equations is detailed. For clarity, the nine equations summarized in table 1 are rewritten in 1-D as

$$\partial_t \mathbf{Y} + \partial_x \boldsymbol{f}(\mathbf{Y}) = \boldsymbol{h}(\mathbf{Y}) + \boldsymbol{s}(\mathbf{Y}). \tag{73}$$

Table 1: Nine-equation macroscale model for monodisperse fluid–particle flow with added mass, internal energy, and PTKE. Gravity $\mathbf{g}$ is included in the model for completeness. Here the $\mathbf{P}_{pfp}$ term is written as a pressure, but it can also be written as a force-coupling term as done in the kinetic model and eqs. (58) and (59). In that case, $\partial_{\mathbf{x}} \cdot \mathbf{P}_{pfp}$ must be added to both sides of the fluid-phase momentum balance, representing the flux and force derived from kinetic theory [22].

Mass balances:

$$\begin{aligned}
\partial_t \rho_p \alpha_p + \partial_{\mathbf{x}} \cdot \rho_p \alpha_p \mathbf{u}_p &= 0 \\
\partial_t \rho_f \alpha_f^\star + \partial_{\mathbf{x}} \cdot \rho_f \alpha_f^\star \mathbf{u}_f &= -S_a \\
\partial_t \rho_e \alpha_p^\star + \partial_{\mathbf{x}} \cdot \rho_e \alpha_p^\star \mathbf{u}_p &= S_a
\end{aligned}$$

Momentum balances:

$$\partial_t \rho_f \alpha_f^\star \mathbf{u}_f + \partial_{\mathbf{x}} \cdot (\rho_f \alpha_f^\star \mathbf{u}_f \otimes \mathbf{u}_f + \hat{p}_f \mathbf{I}) = \alpha_p^\star (\partial_{\mathbf{x}} \hat{p}_f + \mathbf{F}_{pf}) + \frac{\rho_e \alpha_p^\star}{\tau_p} \mathbf{u}_{pf} - \mathbf{S}_{fp} + \rho_f \alpha_f^\star \mathbf{g}$$

$$\partial_t \rho_e \alpha_p^\star \mathbf{u}_p + \partial_{\mathbf{x}} \cdot [\rho_e \alpha_p^\star (\mathbf{u}_p \otimes \mathbf{u}_p + \Theta_p \mathbf{I} + P_p \mathbf{I}) + \mathbf{P}_{pfp}] = -\alpha_p^\star (\partial_{\mathbf{x}} \hat{p}_f + \mathbf{F}_{pf}) - \frac{\rho_e \alpha_p^\star}{\tau_p} \mathbf{u}_{pf} + \mathbf{S}_{fp} + \rho_e \alpha_p^\star \mathbf{g}$$

Fluid-phase energy balances (total and PTKE):

$$\begin{aligned}
\partial_t \rho_f \alpha_f^\star E_f + \partial_{\mathbf{x}} \cdot [\rho_f \alpha_f^\star \mathbf{u}_f E_f + (\alpha_f^\star \mathbf{u}_f + \alpha_p^\star \mathbf{u}_p) \hat{p}_f] = &- \mathbf{P}_{pfp} : (\partial_{\mathbf{x}} \mathbf{u}_p) + \alpha_p^\star \mathbf{u}_p \cdot (\partial_{\mathbf{x}} \hat{p}_f + \mathbf{F}_{pf}) \\
&+ \frac{\rho_e \alpha_p^\star}{\tau_p} [3a\Theta_p - 2(1-a)k_f + \mathbf{u}_{pf} \cdot \mathbf{u}_p] + H_{pf} - S_E + \rho_f \alpha_f^\star \mathbf{u}_f \cdot \mathbf{g} \\
\partial_t \rho_f \alpha_f^\star k_f + \partial_{\mathbf{x}} \cdot \rho_f \alpha_f^\star \mathbf{u}_f k_f = &- \frac{2}{3} \rho_f \alpha_f^\star k_f \partial_{\mathbf{x}} \cdot \mathbf{u}_f + \frac{\rho_e \alpha_p^\star}{\tau_p} [3a\Theta_p - 2(1-a)k_f + u_{pf}^2 - C_f k_f]
\end{aligned}$$

Particle-phase energy balances (kinetic and internal):

$$\begin{aligned}
\partial_t \rho_e \alpha_p^\star K_p + \partial_{\mathbf{x}} \cdot [\rho_e \alpha_p^\star (K_p + \Theta_p + P_p) \mathbf{u}_p + \mathbf{P}_{pfp} \cdot \mathbf{u}_p] = &\, \mathbf{P}_{pfp} : (\partial_{\mathbf{x}} \mathbf{u}_p) - \alpha_p^\star \mathbf{u}_p \cdot (\partial_{\mathbf{x}} \hat{p}_f + \mathbf{F}_{pf}) \\
&- \frac{\rho_e \alpha_p^\star}{\tau_p} [3a\Theta_p - 2(1-a)k_f + \mathbf{u}_{pf} \cdot \mathbf{u}_p] - H_p + S_K + \rho_e \alpha_p^\star \mathbf{u}_p \cdot \mathbf{g} \\
\partial_t \rho_e \alpha_p^\star e_p + \partial_{\mathbf{x}} \cdot \rho_e \alpha_p^\star e_p \mathbf{u}_p = &\, H_p - H_{pf} + S_e
\end{aligned}$$

Table 2: Parameters appearing in macroscale model for monodisperse fluid–particle flow in table 1. In the definition of $\mathbf{R}$, the parameters must satisfy $3B_1 + B_2 > 0$ so that $tr(\mathbf{R}) = u_{pf}^2$ and $C_{pfp} > 0$. The thermodynamic temperatures T_f and T_p are found from the internal energies of their respective phases. λ_f is the fluid-phase thermal conductivity.

$$\kappa = \frac{\rho_e \alpha_p^\star - \rho_p \alpha_p}{\rho_f \alpha_f^\star} \qquad \alpha_f = 1 - \alpha_p \qquad \alpha_a = \frac{\kappa}{1+\kappa}\alpha_f \qquad \alpha_p^\star = \alpha_p + \alpha_a \qquad \alpha_f^\star = \alpha_f - \alpha_a \qquad \mathbf{u}_{pf} = \mathbf{u}_p - \mathbf{u}_f$$

$$\mathbf{R} = \frac{B_1 u_{pf}^2 \mathbf{I} + B_2 \mathbf{u}_{pf} \otimes \mathbf{u}_{pf}}{3B_1 + B_2} \quad \mathbf{P}_{pfp} = C_{pfp}\rho_f \alpha_p^\star \mathbf{R} \quad \mathbf{F}_{pf} = \mathbf{R}\cdot\partial_{\mathbf{x}}\rho_f - (\gamma_f - 1)\rho_f(\partial_{\mathbf{x}}\cdot\mathbf{u}_f)\mathbf{u}_{pf} + C_l \rho_f \mathbf{u}_{pf} \times (\partial_{\mathbf{x}} \times \mathbf{u}_f)$$

$$S_a = \frac{\rho_f}{\tau_a}(c_m^\star \alpha_f \alpha_p - \alpha_a) \qquad \mathbf{S}_{fp} = \max(S_a, 0)\,\mathbf{u}_f + \min(S_a, 0)\,\mathbf{u}_p \qquad S_E = \max(S_a, 0)\,E_f + \min(S_a, 0)\,E_p$$

$$S_K = \max(S_a, 0)\,K_f + \min(S_a, 0)\,K_p \qquad S_e = \max(S_a, 0)\,e_f + \min(S_a, 0)\,e_p \qquad H_{pf} = \frac{6\alpha_p^\star \lambda_f Nu}{d_p^2}(T_p - T_f)$$

$$Re_p = \frac{d_p \nu_{pf}}{\nu_f} \quad Pr_f = \frac{\rho_f C_{p,f} \nu_f}{\lambda_f} \quad Nu = (7 - 10\alpha_f + 5\alpha_f^2)(1 + 0.7 Re_p^{0.2} Pr_f^{1/3}) + (1.33 - 2.4\alpha_f + 1.2\alpha_f^2) Re_p^{0.7} Pr_f^{1/3}$$

$$\nu_{pf} = \frac{\alpha_f^\star}{\alpha_f} u_{pf} \quad c_m^\star = \frac{1}{2}\min(1 + 2\alpha_p, 2) \quad \tau_a = C_a \tau_p \quad \tau_p = \frac{4\rho_e d_p^2}{3\mu_f C_D Re_p} \quad C_D = \frac{24}{Re_p}(1 + 0.15 Re_p^{0.687})\alpha_f^{-2.65}$$

$$\beta = \frac{\rho_e \alpha_p^\star}{\rho_p \alpha_p} \quad \tau_c = \frac{d_p\sqrt{\pi}}{12\alpha_p g_0 \Theta_p^{1/2}} \quad \tau_{fr} = \frac{c_{fr}}{\max(|\partial_{\mathbf{x}}\cdot\mathbf{u}_p|, 1/\tau_c) h_{fr}} \quad g_0 = \frac{1+\alpha_f}{2\alpha_f^3} \quad h_{fr} = \frac{1}{2}\left[1 + \tanh\left(\frac{\alpha_p - \alpha_{max}}{\Delta_{fr}}\right)\right]$$

$$p_f = (\gamma_f - 1)\rho_f e_f - \gamma_f p_{\infty,f} \qquad e_f = E_f - \frac{1}{2}u_f^2 - k_f \qquad \Theta_p = \frac{2}{3}K_p - \frac{1}{3}u_p^2 \qquad H_p = \rho_e \alpha_p^\star \left[\frac{1}{\tau_c}(1 - e_c^2) + \frac{1}{\tau_{fr}}\right]\Theta_p$$

$$\hat{p}_f = p_f + \frac{2}{3}\rho_f k_f \qquad P_p = P_c + P_{fr} \qquad P_c = 2(1 + e_c)\alpha_p g_0 \Theta_p \qquad P_{fr} = \frac{p_{fr}\alpha_p g_0 h_{fr}}{\rho_e \alpha_p^\star}$$

$$T_f = \frac{\gamma_f e_f}{C_{p,f}} \qquad T_p = \frac{e_p}{C_{p,p}} \qquad C_f^{-1} = \alpha_p[1 + 1.25\alpha_f^3 \exp(-\alpha_p \alpha_f^{1/2} Re_p^{1/2})] \qquad \frac{1-a}{1-a_{min}} = \frac{\rho_f}{\rho_p K + \rho_f} \qquad C_{pfp} = c_m^\star$$

Table 3: Example model constants for gas–particle flows. The correlations for B_1 and B_2 are from [55], and are valid for a limited range of Re_p and $\alpha_p > 0.01$. For smaller α_p, B_1 can be taken as constant.

$$B_1 = \max(1.0915 - 0.95 Re_p^{0.02} + 0.01 \ln\alpha_p, -B_2) \qquad B_2 = -\max(0.4046 Re_p^{-0.3} - 0.042, 0)$$

$$e_c = 0.9 \qquad a_{min} = 0.5 \qquad K = 0.06 \qquad C_l = 0.5 \quad C_a = 1$$

$$c_{fr} = 0.01 \qquad \alpha_{max} = 0.63 \qquad \Delta_{fr} = 0.01 \qquad p_{fr} = 533,333 \text{ kg/m/s}^2$$

$$\nu_f = 1.36 \times 10^{-5} \text{ m}^2/\text{s} \qquad \gamma_f = 1.4 \qquad p_{\infty,f} = 0 \text{ kg/m/s}^2 \qquad \lambda_f = 0.03 \text{ kg m/s}^3/\text{K}$$

$$C_{p,f} = 1300 \text{ m}^2/\text{s}^2/\text{K} \qquad C_{p,p} = 900 \text{ m}^2/\text{s}^2/\text{K}$$

The conservative-variable and flux vectors are defined, respectively, as

$$\mathbf{Y} = \begin{bmatrix} \rho_p\alpha_p \\ \rho_f\alpha_f^\star \\ \rho_e\alpha_p^\star \\ \rho_f\alpha_f^\star u_f \\ \rho_e\alpha_p^\star u_p \\ \rho_f\alpha_f^\star E_f \\ \rho_e\alpha_p^\star K_p \\ \rho_f\alpha_f^\star k_f \\ \rho_e\alpha_p^\star e_p \end{bmatrix}, \quad \boldsymbol{f}(\mathbf{Y}) = \begin{bmatrix} \rho_p\alpha_p u_p \\ \rho_f\alpha_f^\star u_f \\ \rho_e\alpha_p^\star u_p \\ \rho_f\alpha_f^\star u_f^2 \\ \rho_e\alpha_p^\star(u_p^2 + \Theta_p + P_p) \\ \alpha_f^\star(\rho_f E_f + \hat{p}_f)u_f \\ \rho_e\alpha_p^\star(K_p + \Theta_p + P_p)u_p \\ \rho_f\alpha_f^\star k_f u_f \\ \rho_e\alpha_p^\star e_p u_p \end{bmatrix}. \tag{74}$$

The non-conservative source-term and the local source-term vectors are defined, respectively, as

$$\boldsymbol{h}(\mathbf{Y}) = \begin{bmatrix} 0 \\ 0 \\ 0 \\ -\alpha_f^\star\partial_x\hat{p}_f + \alpha_p^\star F_{pf} \\ -\alpha_p^\star\partial_x\hat{p}_f - \alpha_p^\star F_{pf} - \partial_x P_{pfp} \\ -\hat{p}_f\partial_x(\alpha_p^\star u_p) + \alpha_p^\star F_{pf}u_p - P_{pfp}\partial_x u_p \\ -\alpha_p^\star u_p\partial_x\hat{p}_f - \alpha_p^\star F_{pf}u_p - u_p\partial_x P_{pfp} \\ -\frac{2}{3}\rho_f\alpha_f^\star k_f\partial_x u_f \\ 0 \end{bmatrix}, \quad \boldsymbol{s}(\mathbf{Y}) = \begin{bmatrix} 0 \\ -S_a \\ S_a \\ D - S_{fp} \\ -D + S_{fp} \\ D_E + H_{pf} - S_E \\ -D_E - H_p + S_K \\ D_{PT} - \rho_e\alpha_p^\star\frac{C_f}{\tau_p}k_f \\ H_p - H_{pf} + S_e \end{bmatrix} \tag{75}$$

where D is the fluid-drag term in the 1-D momentum balances. For simplicity, gravity is not included in the local source terms as it is negligible in the dynamics of high-speed flows.

The separation between non-conservative and local source terms is important as they have different natures. Non-conservative terms are the root of several mathematical and numerical challenges when solving two-fluid systems. Those terms involve derivatives of $\mathbf{Y}$, which play a role in the eigenvalues of the system [34]. Also, it is of primary importance to keep a discrete consistency between $\boldsymbol{f}(\mathbf{Y})$ and $\boldsymbol{h}(\mathbf{Y})$ to prevent pressure disturbances [47]. In this work, the pressure non-disturbing condition is obtained by regrouping pressure terms as in [28]. Then, for the fluid momentum and energy eqs. (62) and (63), respectively, the pressure terms in the fluxes are regrouped with the non-conservative terms as

$$\alpha_p^\star\partial_x\hat{p}_f - \partial_x\hat{p}_f = -\alpha_f^\star\partial_x\hat{p}_f, \quad \alpha_p^\star u_p\partial_x\hat{p}_f - \partial_x(\alpha_p^\star\hat{p}_f u_p) = -\hat{p}_f\partial_x(\alpha_p^\star u_p). \tag{76}$$

The consequence of this rewriting is a pressure-less fluid-momentum flux, which is discussed in section 5.1.3, and a loss of discrete conservation of total energy of both phases as non-conservative terms are no longer compensating. The same is done for P_{pfp}, which can be very stiff close to particle fronts. A robust way to treat it is to regroup terms in the kinetic energy of the particle phase eq. (71) such that

$$P_{pfp}\partial_x u_p - \partial_x(u_p P_{pfp}) = -u_p\partial_x P_{pfp}, \tag{77}$$

which is consistent with the kinetic-theory derivation [22].

The local source term $\boldsymbol{s}(\mathbf{Y})$ can also be challenging to solve numerically because of the potential temporal stiffness [45]. For this reason, the system is split into a hyperbolic operator $\mathcal{H}_{\Delta t}$ containing the conservative fluxes $\partial_x\boldsymbol{f}(\mathbf{Y})$, the non-conservative source term $\boldsymbol{h}(\mathbf{Y})$, and the source-term operator $\mathcal{S}_{\Delta t}$ containing the local source term $\boldsymbol{s}(\mathbf{Y})$ such that integration over a time step Δt leads to

$$\mathbf{Y}^{n+1} = \mathcal{H}_{\Delta t/2}\mathcal{S}_{\Delta t}\mathcal{H}_{\Delta t/2}\mathbf{Y}^n. \tag{78}$$

In the above time integration, a Strang splitting is used to reduce operator-splitting errors. The remainder of this section defines these two discrete operators.

5.1. Numerical treatment of the hyperbolic step

The hyperbolic step $\mathcal{H}_{\Delta t}$ is obtained by applying the Godunov scheme to eq. (73) without source terms [47]:

$$\mathbf{Y}_i^{n+1} = \mathbf{Y}_i^n - \frac{\Delta t}{\Delta x}(\boldsymbol{f}_{i+\frac{1}{2}} - \boldsymbol{f}_{i-\frac{1}{2}}) + \Delta t\, \boldsymbol{h}_i \tag{79}$$

where n and $n+1$ superscripts stand for quantities at time t and $t+\Delta t$, respectively. The subscripts i, $i-\frac{1}{2}$ and $i+\frac{1}{2}$ are the volume average, left-, and right-face, respectively, reconstruction of a quantity defined in the ith computational cell with Δx the cell size.

The computation of spatial fluxes can be tedious because of the discontinuous nature of shocks in the fluid phase and sharp fronts in the particle phase. In [22] a classic HLL scheme was employed to solve for the full system of equations with first-order reconstructions of quantities. While the extension of this scheme to the present nine-equation model is straightforward, and very robust, it introduces excessive diffusion of discontinuities, which can be prohibitive for the accurate simulation of strong shocks or thin particle layers. Also the discretization of non-conservative terms did not allow for mechanical equilibrium.

An improvement can be obtained by considering higher-order reconstructions to better capture discontinuities. In [53], a MUSCL reconstruction with a second-order Runge–Kutta integration in time is applied to a moment method leading to a clear reduction of numerical diffusion. However, this improvement does not cure the severe diffusion of the particle front in our case because of the large disparity in magnitude of the fluid and particle eigenvalues. The particle eigenvalues are usually smaller by several orders of magnitude. When the volume fraction approaches the packing limit, the frictional pressure grows very fast and the resulting particle eigenvalues are higher. This observation is the main motivation for splitting the system into a particle subsystem and a fluid subsystem treated with different flux reconstructions. Interested readers can refer to [3] for a discussion on the sound speed definition in two-phase flows.

In this work, the approach proposed in [28] is used. It consists of a combination of AUSM$^+$up scheme [37] for the particle subsystem, and an HLLC scheme [52] for the fluid sub-system. Specific adjustments are required to obtain a well-posed scheme in the presence of added mass and pfp pressure. As for the HLL scheme used in [22], the numerical fluxes using upwind reconstruction are first order in space, but with enhanced particle front capturing due to the AUSM$^+$up scheme and contact discontinuity capturing in the fluid thanks to the HLLC scheme. A higher-order extension of the scheme is also proposed by using higher-order reconstructions and a multistage integration in time based on the Runge–Kutta method to retrieve a TVD scheme [24]. To achieve the extension to higher order, special care is devoted to the discretization of face quantities and non-conservative terms to retrieve the non-disturbing properties of the scheme.

In the following, the computation of face fluxes for each subsystem is detailed and the non-conservative source term is finally computed accordingly. Note that the extension to higher dimensions is straightforward employing directional splitting. The only issue that needs to be tackled is the potential carbuncle instability produced by the HLLC scheme when a shock is aligned with a Cartesian mesh direction. This can be solved by using a rotational algorithm as in [29].

5.1.1. Reconstruction of left and right states

One major ingredient in the computation of fluxes is the face reconstruction of conservative variables. The superscripts L and R refer to the reconstruction of a quantity at the face $i+\frac{1}{2}$ and stand for left and right states, respectively. For a quantity Φ at face $i+\frac{1}{2}$ and its left-biased high-order approximation $\Phi^{HO,L}_{i+\frac{1}{2}}$, the left reconstruction $\Phi^{L}_{i+\frac{1}{2}}$ is expressed as

$$\Phi^{L}_{i+\frac{1}{2}} = \Phi_i + \frac{1}{2}\Delta x\, s_i^{TVD} \tag{80}$$

with the limited slope s_i^{TVD} defined as [27]

$$s_i^{TVD} = 2\max[0, \min(s_i^L, s_i^R, s_i^{HO})], \quad s_i^L = \frac{\Phi_i - \Phi_{i-1}}{\Delta x}, \quad s_i^R = \frac{\Phi_{i+1} - \Phi_i}{\Delta x}, \quad s_i^{HO} = \frac{\Phi^{HO,L}_{i+\frac{1}{2}} - \Phi_i}{\Delta x} \tag{81}$$

where the high-order face reconstruction $\Phi^{HO,L}_{i+\frac{1}{2}}$ is obtained from WENO5 interpolations [31].

The two-fluid model with added mass needs additional care in the reconstruction of the left and right states. More specifically, the reconstruction of volume fraction and density for both phases needs to be consistent to retrieve a non-disturbing pressure scheme. It is demonstrated in Appendix A that a consistent reconstruction for ρ_e is based on eq. (4):

$$\rho_e^K = \frac{\alpha_p^K}{\alpha_p^{\star,K}}(\rho_p - \rho_f^{HLLC}) + \rho_f^{HLLC} \tag{82}$$

where ρ_f^{HLLC} is the face density obtained from the HLLC scheme detailed in section 5.1.3 and superscript $K = L$ or R. Moreover, the reconstruction of volume fractions must respect

$$\alpha^\star_{f,i+\frac{1}{2}} = 1 - \alpha^\star_{p,i+\frac{1}{2}}. \tag{83}$$

This tight coupling between phases is paramount to the success of the method. In the following sections, all the reconstructed quantities L/R are computed from eq. (80) with the high-order limited slope defined by eq. (81). The only exceptions are ρ_e^L and $\alpha_f^{L,\star}$, which are obtained from eqs. (82) and (83), respectively.

5.1.2. AUSM$^+$up scheme for the particle subsystem

First, the particle subsystem is solved:

$$\mathbf{Y}^{n+1}_{p,i} = \mathbf{Y}^n_{p,i} - \frac{\Delta t}{\Delta x}(\boldsymbol{f}_{p,i+\frac{1}{2}} - \boldsymbol{f}_{p,i-\frac{1}{2}}) \tag{84}$$

with

$$\mathbf{Y}_p = \begin{bmatrix} \rho_p\alpha_p \\ \rho_e\alpha_p^\star \\ \rho_e\alpha_p^\star u_p \\ \rho_e\alpha_p^\star K_p \\ \rho_e\alpha_p^\star e_p \end{bmatrix}, \quad \boldsymbol{f}_p = \begin{bmatrix} \rho_p\alpha_p u_p \\ \rho_e\alpha_p^\star u_p \\ \rho_e\alpha_p^\star(u_p^2 + \Theta_p + P_p) \\ \rho_e\alpha_p^\star(K_p + \Theta_p + P_p)u_p \\ \rho_e\alpha_p^\star e_p u_p \end{bmatrix}. \tag{85}$$

The particle phase has its own equation of state where compressibility is a result of volume-fraction variations:

$$p_p = \rho_e\alpha_p^\star(\Theta_p + P_p) = EOS(\rho_e\alpha_p^\star, \alpha_p, \Theta_p). \tag{86}$$

The compaction wave speed a_p (analogous to the fluid speed of sound) can be computed from [48]

$$a_p = \frac{1}{\rho_p}\sqrt{\rho_p \left.\frac{\partial p_p}{\partial \alpha_p}\right|_{\Theta_p} + \frac{2}{3}\frac{\Theta_p}{\alpha_p^2}\left.\frac{\partial p_p}{\partial \Theta_p}\right|^2_{\alpha_p}}. \tag{87}$$

However, eq. (87) was developed for standard particle systems where pressure is defined such that $p_p = EOS(\alpha_p, \Theta_p)$ with constant ρ_p.

In our model, p_p also depends on fluid quantities, and a_p is computed from the eigenvalues of the particle subsystem to account for added mass. There are three eigenvalues equal to u_p and two eigenvalues that are not necessarily symmetric such that

$$a_p = \max(u_p - \lambda_{p,min}, \lambda_{p,max} - u_p). \tag{88}$$

In gas–particle systems where $\rho_e \approx \rho_p$, computing a_p from eq. (87) or eq. (88) is almost equivalent. However, ρ_e can become several orders of magnitude higher than ρ_p in bubbly flows and a_p needs to be computed from the eigenvalues of the system to avoid stability issues.

The main difficulty arises from the granular pressure p_p in eq. (86), which can take values from zero (low volume fraction) to extremely large (near the packing limit when P_f prevails). In other words, the Riemann solver needs to deal with a pressure-less system and a low-Mach limit, which are both known to cause problems with standard Godunov-type solvers [25]. AUSM-family schemes [38] are perfect candidates to handle the pressure-less limit as they split

the flux into convective and pressure parts, and have the capability to solve near-vacuum flows [36]. Moreover, extra diffusion terms are introduced in the AUSM$^+$up scheme to handle the low-Mach limit [37].

The AUSM$^+$up scheme applied to the particle subsystem leads to the particle flux vector:

$$\boldsymbol{f}_p = \dot{m}_p^\star \boldsymbol{\Psi}_p + \boldsymbol{\Pi}_p \tag{89}$$

with the mass flux $\dot{m}_p^\star = \rho_e \alpha_p^\star u_p$, the quantity vector $\boldsymbol{\Psi}_p = (\rho_p \alpha_p / \rho_e \alpha_p^\star, 1, u_p, K_p, e_p)$, and the pressure flux $\boldsymbol{\Pi}_p = (0, 0, p_p, p_p u_p, 0)$. In the original AUSM scheme [37], the pressure flux is only non-zero for momentum, while enthalpy was transported for energy. In [28], the pseudo-thermal energy Θ_p is solved, and the pressure term for energy is not included in the flux. Here, the kinetic energy K_p is solved and requires to consider a pressure flux consistent between momentum and energy; hence, the unconventional term $p_p u_p$ in $\boldsymbol{\Pi}_p$.

Here, the quantity vector is simply upwinded:

$$\boldsymbol{\Psi}_p = \begin{cases} \boldsymbol{\Psi}_p^L, & \text{if } \dot{m}_p \leq 0 \\ \boldsymbol{\Psi}_p^R, & \text{otherwise} \end{cases} \tag{90}$$

with $\boldsymbol{\Psi}_p^L$ and $\boldsymbol{\Psi}_p^R$ the left and right reconstructions of $\boldsymbol{\Psi}_p$ at a given face. The mass flux $\dot{m}_p^\star$ is computed from the face Mach number $\mathcal{M}_p^{1/2}$ as

$$\dot{m}_p^\star = a_p^{1/2} \mathcal{M}_p^{1/2} \begin{cases} \rho_e^L \alpha_p^{\star,L}, & \text{if } \mathcal{M}_p^{1/2} \leq 0 \\ \rho_e^R \alpha_p^{\star,R}, & \text{otherwise} \end{cases} \tag{91}$$

with $\rho_e^{L/R}$ obtained from eq. (82). The conventional mass flux $\dot{m}_p$ can also be obtained for α_p:

$$\dot{m}_p = a_p^{1/2} \mathcal{M}_p^{1/2} \begin{cases} \rho_p \alpha_p^L, & \text{if } \mathcal{M}_p^{1/2} \leq 0 \\ \rho_p \alpha_p^R, & \text{otherwise} \end{cases}, \tag{92}$$

which corresponds to $(\alpha_p \rho_p / \alpha_p^\star \rho_e) \dot{m}_p^\star$ computed from face reconstructions $\alpha_p^{L/R}$, $\alpha_p^{\star L/R}$, and $\rho_e^{L/R}$. This ensures that α_p and $\alpha_p^\star$ are transported at the same speed.

The face compaction wave speed $a_p^{1/2}$ is computed as in [28] from the following mass average:

$$a_p^{1/2} = \sqrt{\frac{\rho_e^L \alpha_p^{\star,L} (a_p^L)^2 + \rho_e^R \alpha_p^{\star,R} (a_p^R)^2}{\rho_e^L \alpha_p^{\star,L} + \rho_e^R \alpha_p^{\star,R}}} + \epsilon \tag{93}$$

with $\epsilon = 10^{-10}$ a small number to avoid division by zero when the compaction wave speed is null. In the same manner, the face density is defined as

$$\rho_e^{1/2} = \frac{\rho_e^L \alpha_p^{\star,L} + \rho_e^R \alpha_p^{\star,R}}{2}, \tag{94}$$

and the left, right, and averaged Mach numbers are computed from $a_p^{1/2}$:

$$\mathcal{M}_p^L = \frac{u_p^L}{a_p^{1/2}}, \qquad \mathcal{M}_p^R = \frac{u_p^R}{a_p^{1/2}}, \qquad \bar{\mathcal{M}}_p^2 = \frac{(u_p^L)^2 + (u_p^R)^2}{2(a_p^{1/2})^2}. \tag{95}$$

Finally, the face Mach number $\mathcal{M}_p^{1/2}$ related to the convective flux and the face pressure $\mathcal{P}_p^{1/2}$ related to the pressure flux are computed from the split Mach number and pressure polynomials $\mathscr{M}_4^\pm$ and $\mathscr{P}_5^\pm$ [36] as

$$\mathcal{M}_p^{1/2} = \mathscr{M}_4^+(\mathcal{M}_p^L) + \mathscr{M}_4^-(\mathcal{M}_p^R) - \frac{k_p}{f_a} \max(1 - \sigma \bar{\mathcal{M}}_p^2, 0) \frac{p_p^R - p_p^L}{(\rho_e^{1/2} + \epsilon)(a_p^{1/2})^2}, \tag{96}$$

$$\mathcal{P}_p^{1/2} = \mathscr{P}_5^+(\mathcal{M}_p^L) p_p^L + \mathscr{P}_5^-(\mathcal{M}_p^R) p_p^R - 2 k_u f_a \mathscr{P}_5^+(\mathcal{M}_p^L) \mathscr{P}_5^-(\mathcal{M}_p^R) \rho_e^{1/2} (a_p^{1/2} - \epsilon)(u_p^R - u_p^L) \tag{97}$$

with $k_p = 0.25$, $k_u = 0.75$, $f_a = 1$, and $\sigma = 1$ parameters controlling the pressure and velocity diffusion terms. The pressure flux for energy is then computed as $a_p^{1/2}\mathcal{M}_p^{1/2}\mathcal{P}_p^{1/2}$.

5.1.3. HLLC scheme for the fluid subsystem

The fluid subsystem is written as

$$\mathbf{Y}_{f,i}^{n+1} = \mathbf{Y}_{f,i}^{n} - \frac{\Delta t}{\Delta x}(\boldsymbol{f}_{f,i+\frac{1}{2}} - \boldsymbol{f}_{f,i-\frac{1}{2}}) \tag{98}$$

with

$$\mathbf{Y}_f = \begin{bmatrix} \rho_f \alpha_f^\star \\ \rho_f \alpha_f^\star u_f \\ \rho_f \alpha_f^\star E_f \\ \rho_f \alpha_f^\star k_f \end{bmatrix}, \qquad \boldsymbol{f}_f = \begin{bmatrix} \rho_f \alpha_f^\star u_f \\ \rho_f \alpha_f^\star u_f^2 + \hat{p}_f \\ \alpha_f^\star(\rho_f E_f + \hat{p}_f) u_f \\ \rho_f \alpha_f^\star k_f u_f \end{bmatrix}. \tag{99}$$

To solve this system, the particle-phase volume fraction is frozen during a time step and the fluid-phase volume fraction is reconstructed at the face from eq. (83) to ensure consistency between the amount of particles seen from both phases.

While the flux contains the fluid pressure, it does not correspond to a standard Euler step weighted by the volume fraction $\alpha_f^\star$. For this reason, the numerical scheme must be able to compute the reconstruction of fluid pressure apart from the flux, which is not the case for the standard HLL scheme. Hence, the HLLC scheme is used to reconstruct the variables $\mathbf{X}_f = (\rho_f, u_f, \hat{p}_f, E_f, k_f, P_{pfp})$. The pfp pressure P_{pfp} is also included in the reconstructed variables of the fluid system as it appears in the momentum and energy fluxes and is required to compute non-conservative terms for the particle phase.

The HLLC scheme is a three-wave approximate Riemann solver with four intermediate states such that

$$\mathbf{X}_f^{HLLC} = \begin{cases} \mathbf{X}_f^L, & \text{if } 0 \le S^L \\ \mathbf{X}_f^{L\star}, & \text{if } S^L \le 0 \le S^\star \\ \mathbf{X}_f^{R\star}, & \text{if } S^\star \le 0 \le S^R \\ \mathbf{X}_f^R, & \text{if } S^R \le 0 \end{cases} \tag{100}$$

with $\mathbf{X}_f^K$ left ($K = L$) and right ($K = R$) states reconstructed at the face, and $\mathbf{X}_f^{K\star}$ the intermediate states at the left and right sides of the contact wave computed as described below. In the standard HLLC method, the left and right wave speed S^K are reconstructed as in HLL [15] or from the Roe-average [16]. In our solver, they are retrieved from the minimum and maximum eigenvalues of the fluid system in eq. (98), which accounts for added mass, and the contact wave speed $S^\star$ is computed as in [1]:

$$S^L = \lambda_{f,min}, \quad S^R = \lambda_{f,max}, \quad S^\star = \frac{\hat{p}_f^R - \hat{p}_f^L + \rho_f^L u_f^L (S^L - u_f^L) - \rho_f^R u_f^R (S^R - u_f^R)}{\rho_f^L (S^L - u_f^L) - \rho_f^R (S^R - u_f^R)}. \tag{101}$$

The contact pressure can then be computed as

$$\hat{p}_f^\star = \frac{1}{2}[\hat{p}_f^L + \hat{p}_f^R + \rho_f^L (S^L - u_f^L)(S^\star - u_f^L) + \rho_f^R (S^R - u_f^R)(S^\star - u_f^R)]. \tag{102}$$

Finally, the left and right states apart from the contact wave can be computed as $\mathbf{X}_f^{K\star} = (\rho_f^{K\star}, S^\star, \hat{p}_f^\star, E_f^{K*}, k_f^K, P_{pfp}^K)$, such that

$$\rho_f^{K\star} = \rho_f^K \frac{S^K - u_f^K}{S^K - S^\star}, \quad E_f^{K\star} = E_f^K + \frac{S^\star \hat{p}_f^\star - S^K \hat{p}_f^K}{\rho_f^K (S^K - u_f^K)}. \tag{103}$$

The scheme results in an upwinding of P_{pfp}. This is a key component of the method to ensure stability of the model as P_{pfp} is also discontinuous across a particle front. While this term is not significant in dense gas–particle systems, it needs to be treated carefully for bubbly flows.

The fluid fluxes are finally assembled using $\alpha^\star_f$ and $\mathbf{X}^{HLLC}_f$ at face $i+\frac{1}{2}$ such that

$$\boldsymbol{f}_{f,i+\frac{1}{2}} = \begin{pmatrix} \alpha^\star_{f,i+\frac{1}{2}}\rho_{f,i+\frac{1}{2}}u_{f,i+\frac{1}{2}} \\ \alpha^\star_{f,i+\frac{1}{2}}\rho_{f,i+\frac{1}{2}}u_{f,i+\frac{1}{2}}u_{f,i+\frac{1}{2}} + \hat{p}_{f,i+\frac{1}{2}} \\ \alpha^\star_{f,i+\frac{1}{2}}\rho_{f,i+\frac{1}{2}}E_{f,i+\frac{1}{2}}u_{f,i+\frac{1}{2}} + \alpha^\star_{f,i+\frac{1}{2}}u_{f,i+\frac{1}{2}}\hat{p}_{f,i+\frac{1}{2}} \\ \alpha^\star_{f,i+\frac{1}{2}}\rho_{f,i+\frac{1}{2}}k_{f,i+\frac{1}{2}}u_{f,i+\frac{1}{2}} \end{pmatrix}. \tag{104}$$

5.1.4. Non-conservative terms

Finally the non-conservative terms are reconstructed. It has been shown in the literature that the discretization of those terms need to be defined carefully to be compatible with the flux reconstruction. In practice, the face reconstructions defined in eq. (100) are used to compute $\boldsymbol{h}(\mathbf{Y})$ such that

$$\partial_x \hat{p}_f = \frac{\hat{p}_{f,i+\frac{1}{2}} - \hat{p}_{f,i-\frac{1}{2}}}{\Delta x},\ \ \partial_x u_f = \frac{u_{f,i+\frac{1}{2}} - u_{f,i-\frac{1}{2}}}{\Delta x},\ \ \partial_x u_p = \frac{u_{p,i+\frac{1}{2}} - u_{p,i-\frac{1}{2}}}{\Delta x},\ \ \partial_x P_{pfp} = \frac{P_{pfp,i+\frac{1}{2}} - P_{pfp,i-\frac{1}{2}}}{\Delta x}. \tag{105}$$

Note that in multi-dimensional cases, the curl velocity $\partial_{\mathbf{x}} \times \mathbf{u}_f$ needed for the lift force is computed from the reconstructed variables.

5.1.5. Time integration of the hyperbolic step

All the terms described in the previous sections can be assembled to constitute the hyperbolic step $\mathcal{H}_{\Delta t}$ with the final discretization given in Appendix A. In order to remain stable with WENO5 reconstructions, a RK3-SSP scheme is employed that also preserves realizability [53] and the time integration proceeds as follows [50]:

$$\begin{aligned} \mathbf{Y}^{(1)} &= \mathbf{Y}^n - \Delta t\, \partial_x \boldsymbol{f}(\mathbf{Y}^n) + \Delta t\, \boldsymbol{h}(\mathbf{Y}^n), \\ \mathbf{Y}^{(2)} &= \frac{3}{4}\mathbf{Y}^n + \frac{1}{4}[\mathbf{Y}^{(1)} - \Delta t\, \partial_x \boldsymbol{f}(\mathbf{Y}^{(1)}) + \Delta t\, \boldsymbol{h}(\mathbf{Y}^{(1)})], \\ \mathbf{Y}^{n+1} &= \frac{1}{3}\mathbf{Y}^n + \frac{2}{3}[\mathbf{Y}^{(2)} - \Delta t\, \partial_x \boldsymbol{f}(\mathbf{Y}^{(2)}) + \Delta t\, \boldsymbol{h}(\mathbf{Y}^{(2)})]. \end{aligned} \tag{106}$$

The overall time step is based on the maximum particle and fluid eigenvalues. The eigenvalues are more complicated than for the standard Baer–Nunziato equations and are found numerically using a subroutine for the Jacobian matrix that was generated symbolically. Hyperbolicity of the system has been demonstrated in [22].

5.2. Numerical treatment of local source terms

The remaining part of the full system is the local source term $\boldsymbol{s}(\mathbf{Y})$. The approach here is to use a time splitting of the different relaxation mechanisms sorted by timescale. This results in solving a succession of linear ODEs that can be solved analytically. A first advantage of this approach is to impose strict conservation of quantities during the integration time. Also, it alleviates the time constraint, which can be very restrictive in the case of dramatic shocks interacting with a dispersed phase. For each term, a separate semi-analytical solution is derived and used to update the conserved variables in each phase. The semi-analytical solutions of drag $\mathcal{S}^D$, added-mass $\mathcal{S}^{AM}$, heat transfer $\mathcal{S}^{HT}$ and particle collision–friction $\mathcal{S}^{CF}$ are detailed in Appendix B.

The local source term operator is then written as:

$$\mathcal{S}_{\Delta t} = \mathcal{S}^{CF}_{\Delta t}\mathcal{S}^{D}_{\Delta t}\mathcal{S}^{HT}_{\Delta t}\mathcal{S}^{AM}_{\Delta t} \tag{107}$$

with Δt the time step from the hyperbolic step.

6. Numerical examples

This section consists of various 1-D test cases to assess the solver's capabilities to handle a large range of Mach numbers, volume fractions, and material-density ratios between the fluid and particles. For this purpose, the fluid can

Table 4: Default physical properties of the fluids used for test cases.

Fluid	γ_f	$p_{\infty,f}$ (GPa)	ν_f (Pa·s)	$C_{p,f}$ (J/kg/K)	λ_f (m^2/s)
Air	1.4	0	$2.12 \cdot 10^{-5}$	1005	$2.56 \cdot 10^{-2}$
Water	4.4	0.6	10^{-6}	5250	$6 \cdot 10^{-2}$

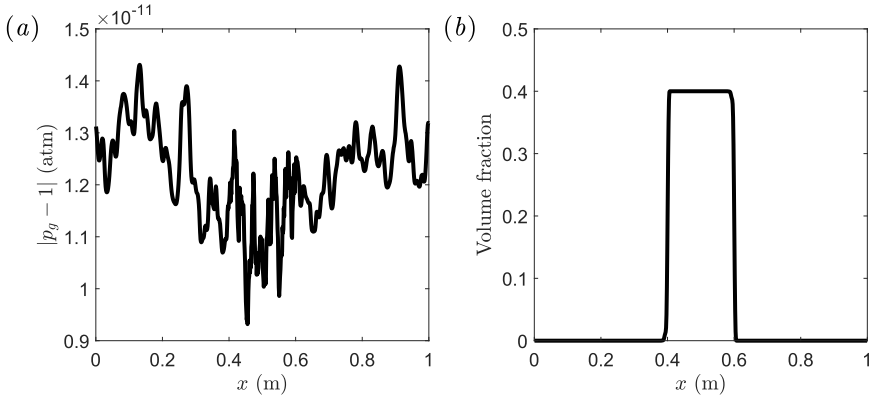

Figure 2: Gas-phase pressure (a) and particle volume fraction (b) for the mechanical equilibrium after one box length travel with $N_x = 800$.

be either air or water with properties given in table 4. The particle phase can be solid particles or non-deformable spherical bubbles with properties provided in the corresponding test case. In the solver, the minimum value of the particle-phase volume fraction α_ϵ is set at a small value (10^{-12}) to avoid division by zero. Therefore, the quantities for the disperse phase are only displayed when $\alpha_p > 10^{-8}$ to provide meaningful values. In all test cases, if not specified, the model parameters take the values $e_c = 1$, $\Delta_f = 0.01$, $\alpha_{max} = 0.65$ and $C_{pfp} = c_m^\star$ and the CFL number takes the value of 0.5.

In general, for gas–particle test cases, the model formulation, numerical solver, and results are very similar to those reported in [28]. In contrast, the bubbly flow cases are more challenging for the hyperbolic solver because of the strong phase coupling due to buoyancy and added mass. Unlike for gas–particle flows wherein the largest eigenvalues can arise in the particle phase, this does not occur for bubbly flows. Nonetheless, complex eigenvalues are likely to arise in bubbly flow due to buoyancy when the pfp pressure P_{pfp} is too small, leading to nonphysical behavior of the macroscale model [22]. For the model proposed in this work, this behavior is avoided since $C_{pfp} = c_m^\star \geq 0.5$.

6.1. Assessment of the hyperbolic solver

In this section, we verify that the proposed solver satisfies a few basic properties of the continuum mode.

6.1.1. Mechanical equilibrium of a moving particle dust

First, the pressure non-disturbing condition is demonstrated on the advection of a dust cloud in air with equal velocities $u_p = u_f = 100$ m/s, equal temperatures $T_p = T_f = 300$ K and fluid pressure taken as $p_f = 1$ atm. For mechanical equilibrium to be retrieved, Θ_p and k_f are set to zero. The dust cloud of width 0.2 m and $\alpha_p = 0.4$ is centered in a periodic domain with length $L = 1$ m. In fig. 2, the pressure errors and the volume fractions are displayed after one box length travel with a grid refinement of $N_x = 800$. The pressure errors are of order 10^{-11}, which demonstrates the consistency of the hyperbolic system discretization.

6.1.2. Mesh convergence on a two-phase shock tube

The computational scheme is next compared to the first-order HLL scheme employed in [22]. A first-order version of the present scheme is also studied to compare the features of the schemes setting aside the order of reconstruction of the quantities. The first-order version of the scheme then uses Euler integration in time and a reconstruction from eq. (80) with first-order slope limiter $s_i^{TVD} = 0$. The first-order and high-order versions of the new scheme will be referred as NFO and NHO, respectively. The verification test case is taken from [28] where a strong shock interacts

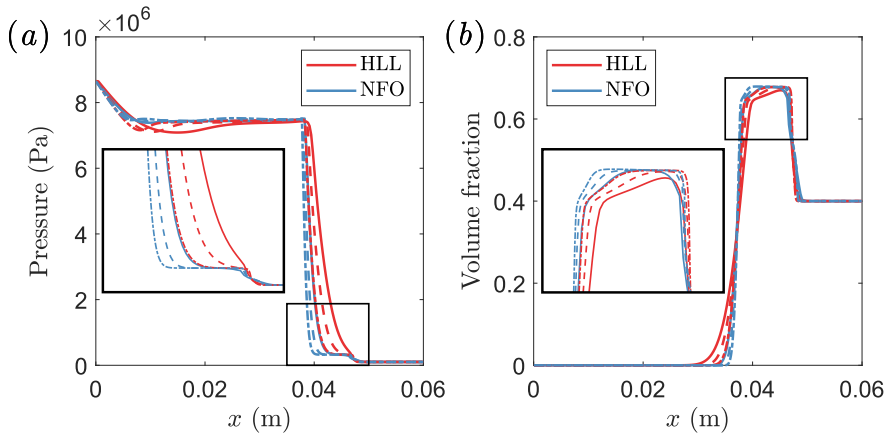

Figure 3: Gas-phase pressure (a) and particle volume fraction (b) for the dense shock tube case at $t = 100$ µs using HLL (red) and NFO (blue). The three levels of grid refinement are $N_x = 200$ (——), 400 (- - -) and 800 (-···-).

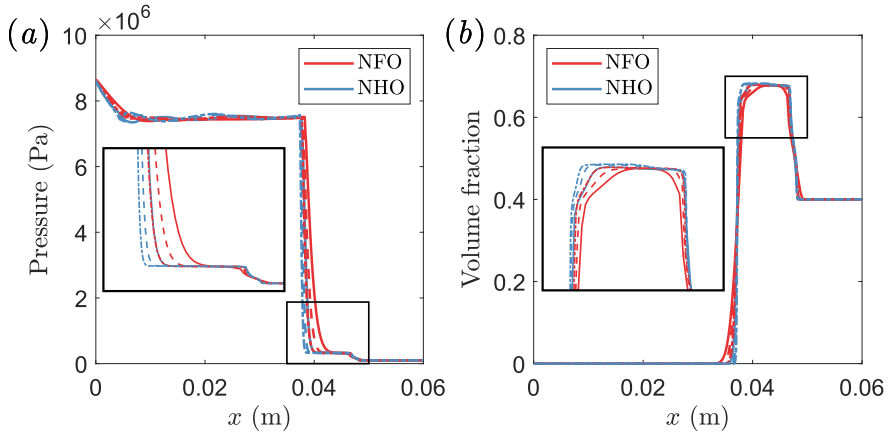

Figure 4: Gas-phase pressure (a) and particle volume fraction (b) for the dense shock tube case at $t = 100$ µs using NFO (red) and NHO (blue). The three levels of grid refinement are $N_x = 200$ (——), 400 (- - -) and 800 (-···-).

with a dense particle cloud. It consists of a shock tube where the left chamber contains pure high-pressure air, while the right chamber is filled with a mixture of air and particles. Hence, the case allows to test capability of the solver to capture a shock, a contact discontinuity and a particle front in the presence of strong dynamics.

The particle concentration is chosen to be high, such that the volume-fraction front approaches the packing limit as the shock pushes the particle phase to the right of the domain. The method should be able to remain stable when P_{fr} controls the eigenvalues. Moreover, the strong shock creates a sudden heating of the gas that is partially absorbed by the particle phase, which has the effect of greatly weakening the shock. The computational domain length is $L = 0.06$ m, and the left and right states are separated by a diaphragm located at $x = 0.03$ m. Solid particles are defined with $\rho_p = 1470$ kg/m^3, $d_p = 5$ µm, and $C_{p,p} = 987$ J/kg/K. The left and right states for the gas are $p_f^L = 100$ atm, $p_f^R = 1$ atm, $T_{f,p}^L = T_{f,p}^R = 300$ K, $\alpha_f^L = 1$, and $\alpha_f^R = 0.6$. The three schemes are compared for three levels of grid refinement: $N_x = 200$, 400, and 800.

The fluid pressure and particle volume fraction at $t = 100$ µs are shown in fig. 3 for HLL versus NFO, and in fig. 4 for NFO versus NHO. It is clear from both the pressure and volume fraction that the new scheme combining AUSM$^+$up and HLLC is better at capturing discontinuities. Even though first-order reconstructions are used in fig. 3, the new scheme is able to capture the particle front accurately. More quantitatively, the HLL scheme requires $N_x = 800$ to give the same degree of detail compared to NFO with $N_x = 200$ on this test case. The same can be observed for NFO with $N_x = 800$ which gives comparable results with the NHO with $N_x = 200$. Overall, all schemes converge

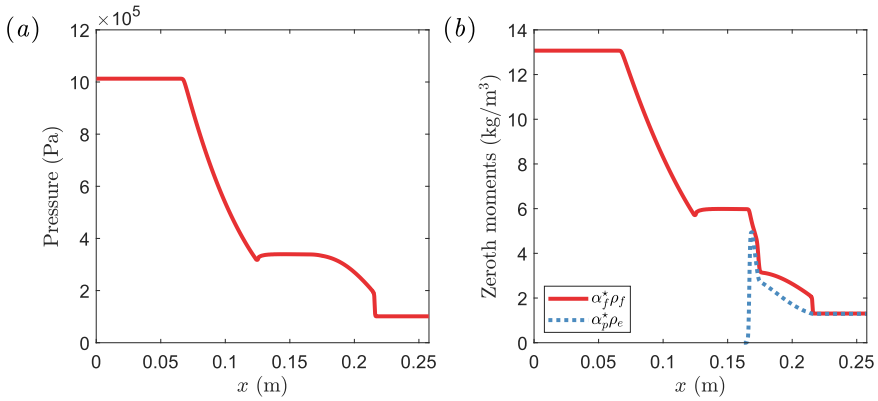

Figure 5: Gas-phase pressure (a) and mass densities (b) for the dilute shock tube at $t = 184$ µs.

with mesh refinement while NHO captures correctly discontinuities even with a coarse grid.

Now that the proposed scheme has been verified and mesh convergence has been assessed on a demanding test case, the remaining numerical examples are computed using the high-order scheme NHO with the highest mesh refinement: $N_x = 800$.

6.2. Air shock wave interacting with a particle cloud

In this example, a dilute shock tube and the dense shock tube presented above are investigated. In general, gas–particle flows are simpler to simulate than bubbly flows due to relatively small effect of buoyancy. However, due to differences in the model formulation (e.g., the frictional source and pfp pressure), results from the two-fluid model in table 1 can be expected to exhibit some differences with the model in [28] for gas–particle flows.

6.2.1. Dilute shock tube

For this example, the right state contains a very dilute particle phase such that the solver must handle an almost pressure-less system. The domain length is $L = 0.257798$ m and the left and right states are separated by a diaphragm located at $x = 0.129$ m to reproduce the same setup as in [28]. Even though no exact solution exists for this case, results can be compared to the results presented in [28]. Solid particles are defined with $\rho_p = 2500\,\mathrm{kg/m^3}$, $d_p = 10\,\mu\mathrm{m}$, and $C_{p,p} = 720$ J/kg/K. The left and right states are $p_f^L = 10$ atm, $p_f^R = 1$ atm, $T_{f,p}^L = T_{f,p}^R = 270$ K, $\alpha_p^L = 0$, and $\alpha_p^R = 5.172 \cdot 10^{-4}$. The quantities of interest are plotted at $t = 184$ µs in fig. 5.

As the shock progresses in the gas–particle mixture, it experiences momentum and heat loss because of the drag force and heat transfer. As noted in [28], the hook-like structure of $\hat{p}_f$ near the initial shock position is well captured. The main difference with [28] is the profile of particle mass density near $x = 0.15$, which is higher with our model. This is likely due to the unsteady force F_{pf} that accelerates the particles near the shock and contact surface. Overall, the physical behavior is retrieved and showcases the performance of the proposed scheme near pressure-less conditions.

6.2.2. Dense shock tube

The problem introduced in section 6.1 is repeated with more details to better describe the weakening of the shock, the balance of particle pressure in the dense part of the granular phase, and the effect of drag on phase velocities. In fig. 6, the phase pressures, velocities, temperatures and mass densities are provided. The solutions agree well with [28], apart from the granular pressure, which experiences an abrupt decrease at the particle front. By plotting the collisional and frictional parts of the particle-phase pressure (which are clearly separated at $\alpha_p = \alpha_{max}$), it can be seen that the frictional pressure is controlling where the volume fraction approaches the packing limit, but decreases abruptly at the particle front. This behavior is due to the different functional forms used for the frictional pressure in the present model compared to what was used in [28]. By increasing the parameter Δ_f, the transition zone is larger and frictional pressure is applied at lower volume fractions. The temperature profiles showcase the heating of particles

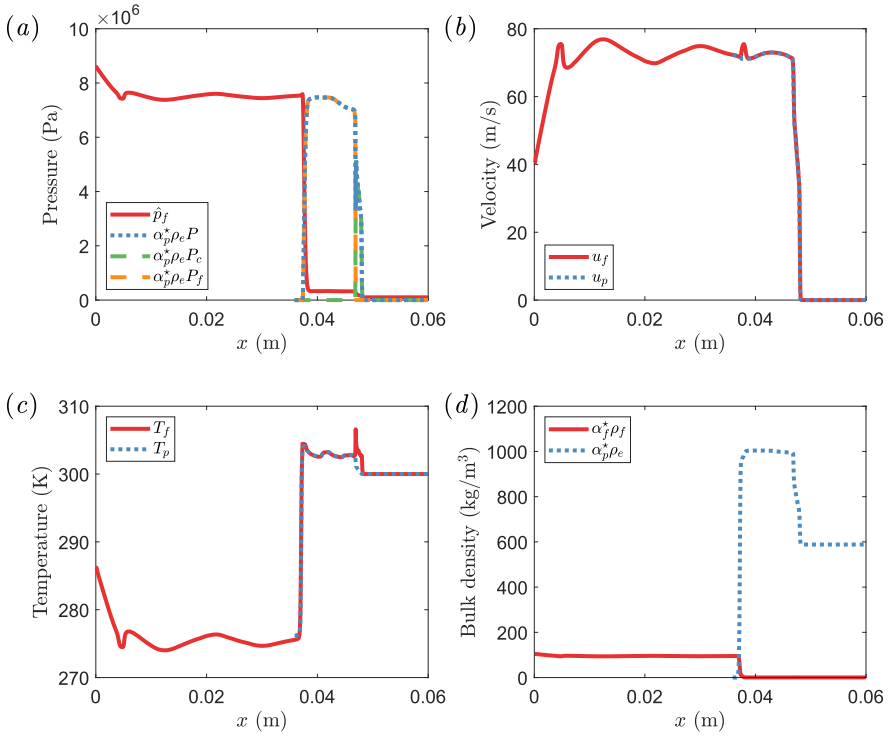

Figure 6: Pressures (*a*), velocities (*b*), temperatures (*c*), and mass densities (*d*) for the dense shock tube at $t = 1$ ms.

Table 5: Physical properties of the fluid and particle phases for particle-curtain cases.

Configuration	Material	ρ_p (kg/m^3)	d_p (µm)	δ_0 (mm)	α_p	$\mathcal{M}_s$
1	316 stainless steel	8170	115	1.7	0.17	1.4
2	Tungsten	17070	115	2.3	0.18	1.55
3	Cast stainless steel	7390	328	4.0	0.09	1.7
4	Soda lime glass	2420	115	2.0	0.19	4.24

through the shock, which explains the weakening of the shock with an amount equivalent to what was observed in [28].

Finally, it is interesting to notice that the present model is stable and without particle-pressure oscillations, even when $e_c = 1$. In [28], strong oscillations were observed and additional dissipation was needed in the numerical scheme to control them. In the current model, the granular temperature Θ_p is strongly damped to negligible values in the frictional regime by the frictional source term included in H_p, a term that is not present in [28]. Moreover, we use a sharper cut-off between the frictional and collisional regimes in the definition of P_{fr} (see individual particle pressure contribution in fig. 6(a)), and compute the particle-phase eigenvalues directly from the Jacobian matrix. As a result, the proposed hyperbolic solver is robust with $e_c = 1$ without additional dissipation even when $\alpha_p > \alpha_{max}$.

6.3. Shock-induced dispersal of particle curtains

Next, the gas–particle solver is validated against experimental data. The most commonly used experiment is the interaction of a shock with a particle curtain. Usually solutions are compared with the famous experiment of Rogue et al. [46]. Here, the recent experiments of Daniel et al. [11] are reproduced with volume fractions ranging from $\alpha_p = 0.09$ to 0.2, Mach number of the air shock ranging from $\mathcal{M}_f = 1.4$ to 1.7, and four particles with different densities and diameters. A recent hypersonic configuration with $\mathcal{M}_f = 4.24$ from the same group [54] is also simulated. The four configurations are summarized in table 5.

The computational domain is $[-L/2, L/2]$ with $L = 0.2$ m, non-reflective boundary conditions are used to match the experiments and $N_x = 2000$ is used. The shock is produced by a fluid pressure ratio with the diaphragm located upstream of the curtain at $x_d = -L/4$. The fluid pressure ratio between driver (state 2) and driven (state 1) chambers are related to the shock Mach number $\mathcal{M}_s$:

$$\frac{p_2}{p_1} = \frac{1 + \frac{2\gamma_1}{\gamma_1+1}(\mathcal{M}_s^2 - 1)}{\left(1 - \frac{\gamma_2-1}{\gamma_1+1}\frac{c_1}{c_4}\frac{\mathcal{M}_s^2-1}{\mathcal{M}_s}\right)^{\frac{2\gamma_2}{\gamma_2-1}}}. \tag{108}$$

The driver gas is not expected to be relevant for the interaction with the particle curtain and has been taken as air, while nitrogen was used in the experiments [11]. The driven air is at ambient conditions $T_1 = 297$ K and $p_1 = 84.1$ kPa. The driver air temperature is also taken at $T_2 = 297$ K. Example results obtained with the solver are represented in fig. 7a where an x–t diagram of density with isocontours of α_p are plotted. When the diaphragm is released, a contact wave and a shock wave are created and propagate towards the curtain. The time is defined such that $t = 0$ represents the moment where the shock hits the upstream edge of the curtain. Then a part of the shock wave is transmitted, while a reflected shock wave travels back upstream. Complex patterns are then generated by the combination of the initial contact wave and reflected shock wave.

The spreading rate is compared with the experiments where all four configurations are displayed in fig. 7b. It can be observed that the results compare fairly well with the experiments, but with deviations when the Mach number increases. This can hide an underlying relation between drag and Mach number, which can be modeled for hard spheres [39]. A detailed study of the effect of the drag model on the physical behavior of the particles is outside the scope of this paper.

Another explanation for the difference between the numerical and experimental results can be due to the value of C_{pfp}, which has been taken equal to $c_m^\star$. This coefficient controls the magnitude of the pfp pressure, which can have a strong implication on the spreading of the particles in the curtain, especially for high Mach numbers with large slip velocity. To investigate this model parameter, the first configuration has been simulated with different values of C_{pfp}

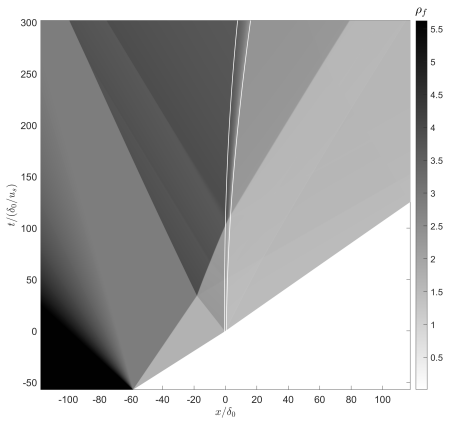

(a) x–t diagram of density with isocontours of α_p (white) for configuration 1.

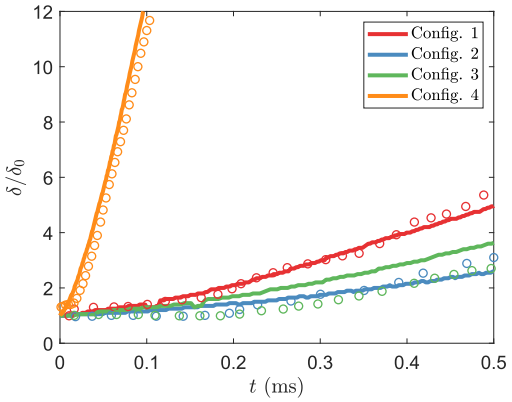

(b) Comparison of the results obtained by the experiment (symbols) and the numerical results (solid lines) for the four configurations detailed in table 5.

Figure 7: Shock-induced dispersal of particle curtains illustrated with the x–t diagram of density (left) and the comparison of the spreading rate with experimental data (right).

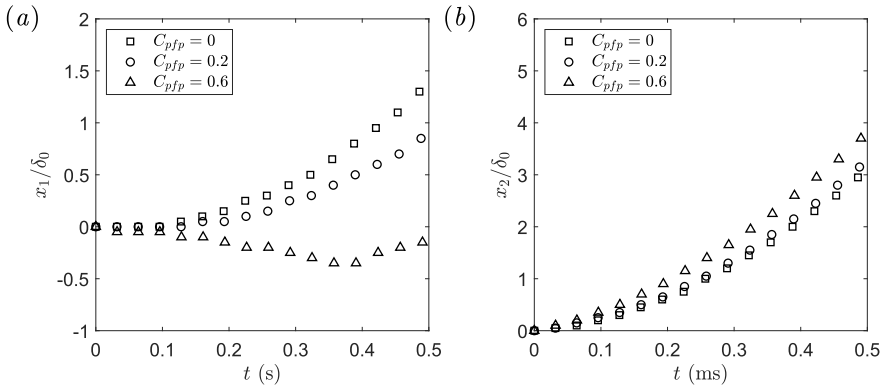

Figure 8: Comparison of upstream edge position x_1 (a) and downstream edge position x_2 (b) for different values of C_{pfp} in configuration 1.

Table 6: Two configurations from [2] tested for a water shock in a fixed particle array. τ corresponds to the transit time d_p/u_s.

Configuration	$\mathcal{M}_s$	α_p	p_f^L (MPa)	ρ_f^L (kg/m^3)	u_f^L (m/s)	τ (ns)
LM10	1.22	0.1	477.73	1136.1	241.2	50.39
HM20	3	0.2	7823.7	1487.8	1606.5	20.49

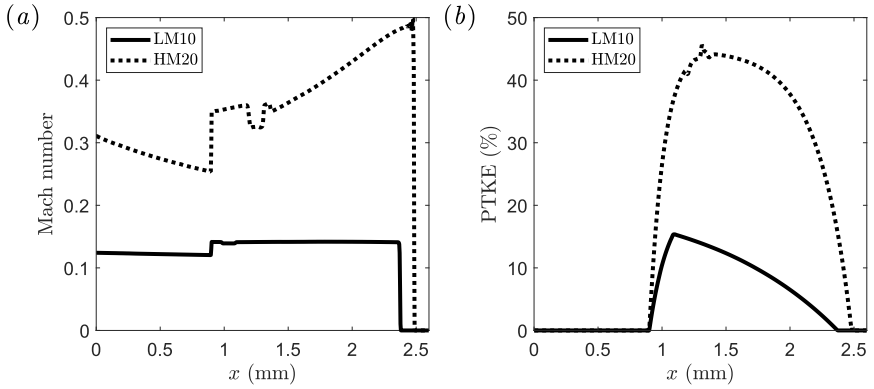

Figure 9: Mach number (a) and PTKE (b) for the two configurations LM10 and HM20 at $t = 16\tau$.

ranging from 0 to 0.6 and the related spreading rates are plotted in fig. 8. The results illustrate the impact of C_{pfp} on the granular phase dynamics. When the pfp-pressure magnitude is increased using C_{pfp}, the upstream edge position x_1 is highly impacted. The curtain can even go backward in the case of $C_{pfp} = 0.6$, while the upstream edge does not move as much when C_{pfp} is set to zero. For the downstream edge location x_2, the difference is not as significant and all three curves almost collapse.

6.4. Underwater shock wave in a fixed particle array

Now that gas–particle systems have been investigated, the interaction of an underwater shock with fixed particles is considered. The main particularity of a water shock compared to a gas shock is that the resulting post-shock Mach number is subsonic. The setup is based on the PRDNS study presented in [2] where a random array of fixed particles is defined in a part of the domain and a strong shock is initialized upstream of the array. In the model, the particle density is fixed at $\rho_p = 10^9$ kg/m^3 to make sure that the position of the granular phase remains fixed. However, $\alpha_p^\star$ is still able to vary because of the added mass. The mean particle diameter is $d_p = 100$ µm and heat transfer is deactivated as in the PRDNS. The domain is taken as $L = 26d_p$, while the particle array is located at $x_p = 9d_p$ and extends until the right end of the domain. The shock is initially positioned one diameter before the particle array $x_s = 8d_p$.

In [2], two Mach numbers and two volume fractions are simulated, leading to four configurations. Here, the two configurations, referred as LM10 and HM20, are tested and compared to the PRDNS results. The volume fraction and post-shock (left) state corresponding to the two configurations are summarized in table 6. The pre-shock (right) state is defined as $p_f^R = 1$ atm, $\rho_f^R = 998.0$ kg/m^3. The simulations stop at $t = 16\tau$ with $\tau = d_p/u_s$ the transit time. In the simulations, large fluctuations of the fluid velocity (corresponding to PTKE) can be observed for HM20, while only small interactions with the particle array are observed for LM10. To compare with the PRDNS results, the Mach number u_f/a_f and dimensionless PTKE $2k_f/u_f^2$ are shown in fig. 9.

The velocity fluctuations, corresponding to PTKE in the model, are well reproduced in the 1-D simulation wherein the dimensionless PTKE reaches 50% for HM20. The results compare well with the Mach contour provided in [2] where reflections are only observed for HM20. In fig. 10, the volume fractions of particle phase α_p and particle with added mass $\alpha_p^\star$ are also presented. It is interesting to notice that α_p remains constant, as particle material density is very high. However, $\alpha_p^\star$ increases in the particle phase as a result of fluid-density variations. This added-mass rise has an impact on the mean and fluctuating velocities of the fluid. Indeed, a bump of Mach and a spike in PTKE can be observed in fig. 9 at the exact location where added mass increases. This illustrates the effects of added mass even

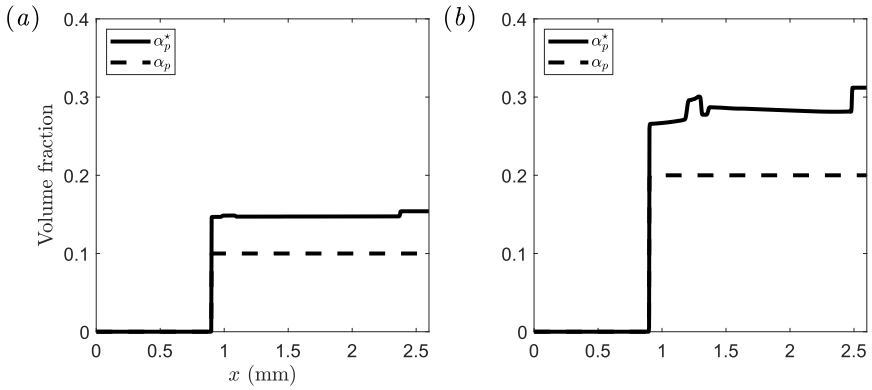

Figure 10: Volume fractions α_p and $\alpha_p^\star$ for the two configurations LM10 (*a*) and HM20 (*b*) for at $t = 16\tau$.

for a case where the particle locations are fixed. The predicted magnitude of this effect can be modified using the parameter C_a in the definition of added-mass relaxation timescale τ_a.

6.5. Shock wave in a bubbly flow

The final numerical example is adapted from the shock tube test cases of section 6.2, but the fluid is now water and the particle phase has a low material density such that it mimics non-deformable spherical bubbles. The domain length is $L = 1$ m and the left and right states are separated by a diaphragm located at $x = 0.5$ m to reproduce the same setup as in [23]. Particles are defined with $\rho_p = 1$ kg/m^3, $d_p = 500$ µm, and $C_{p,p} = 987$ J/kg/K. The left and right states are taken as $p_f^L = 10^9$ Pa, $p_f^R = 10^5$ Pa, $\rho_f^L = \rho_f^R = 1000$ kg/m^3. The left state is pure water, while the right state corresponds to a bubbly flow with different aeration levels α_p^R. Note that a proper bubble model would use the internal bubble pressure to determine the bubble diameter and material density. Nevertheless, the setup is still relevant to show the capability of the solver to handle large material-density ratios between the fluid and particles, and the resultant slip velocity. In such systems, the buoyancy terms become important and hyperbolicity is only preserved thanks to the pfp pressure [22]. For this reason, the C_{pfp} coefficient needs to be at least 0.085 to guarantee global hyperbolicity[4] of the two-fluid model for bubbly flow [22].

6.5.1. Low aeration

As done for the gas–particle system, a first test is defined with a low volume fraction of $\alpha_p^R = 10^{-4}$. The pressure and phase velocities at $t = 79$ µs are displayed in fig. 11. As expected, the bubble swarm is too dilute to impact the water shock. The shock wave then crosses the bubble swarm without decelerating. From the velocity profiles, it is interesting to notice that the slip velocity is especially large compared to the gas–particle systems. This is due to the predominant buoyancy terms in bubbly flows. At the shock front, the pressure gradient is very large and creates a strong acceleration of the bubble swarm. The bubble velocity subsequently relaxes back to the fluid velocity behind the shock due to drag. Similar, but not as strong, behavior is observed for smaller bubbles. As expected, the predicted values of Θ_p are small in bubbly flows due to the small Stokes number.

6.5.2. High aeration

In this case, the same setup is used with a volume fraction of $\alpha_p^R = 0.4$. The fluid pressure, phase velocities, temperatures and mass densities at $t = 79$ µs are displayed in fig. 12. In contrast to the gas–particle dense case, the shock is not weakened by the dense bubble swarm. On the contrary, it is accelerated because of the reduction of cross section experienced by water as α_p increases. However, the same velocity peak observed in gas–particle flows appears at the upstream edge of bubble swarm. Finally, the pressure gradient is smoothed at the shock front, which does not

[4]Global hyperbolicity requires real eigenvalues for all physical values of the conversed variables. For example, the system can be locally hyperbolic with $C_{pfp} = 0$ if Θ_p is sufficiently large.

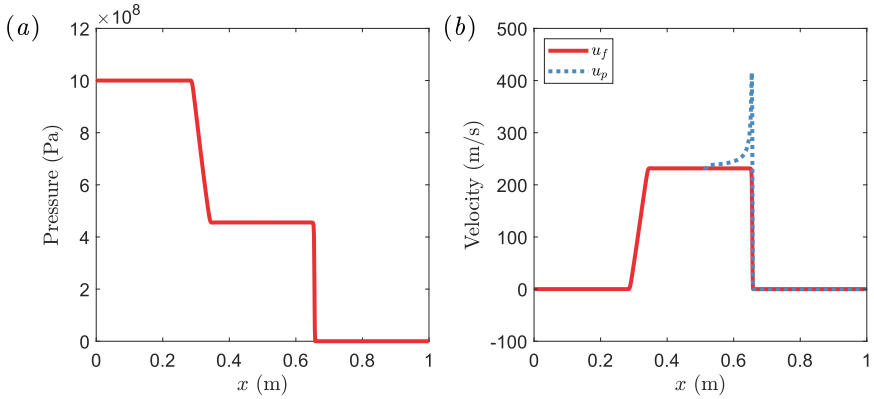

Figure 11: Fluid pressure (a) and phase velocities (b) for low aeration at t = 79 µs.

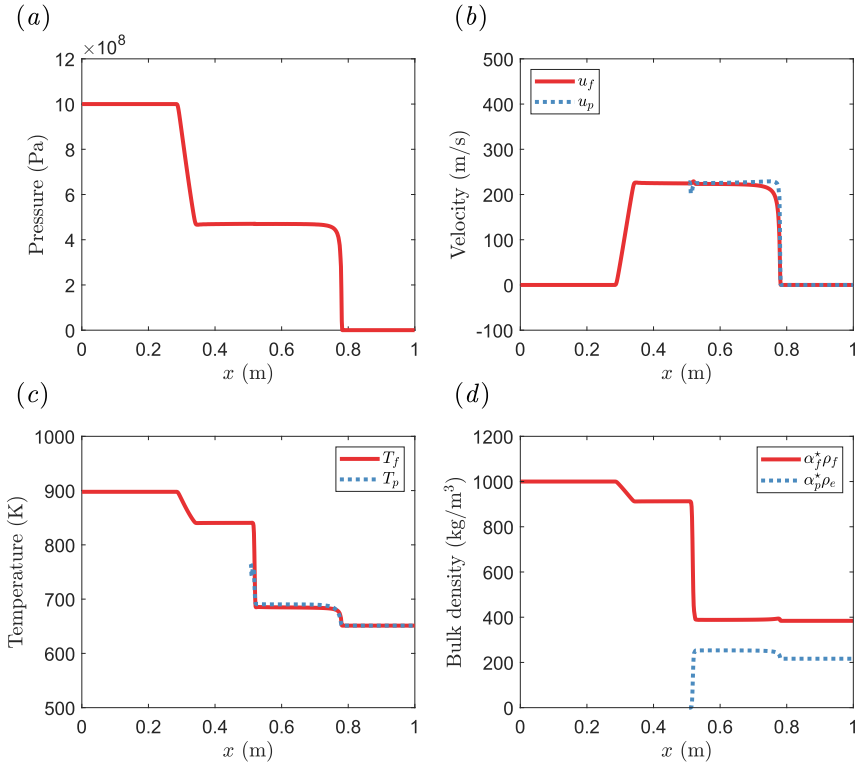

Figure 12: Fluid pressure (a), velocities (b), temperatures (c), and mass densities (d) for high aeration at t = 79 µs.

produce an acceleration comparable to the dilute case. As a result, the bubble volume fraction does not increase significantly as was observed for the heavy particles. This last test case demonstrates the capability of the solver to simulate water–bubble systems where added mass and buoyancy terms are predominant. In gravity-driven systems, large volume-fraction regions (e.g., foams) can be produced, leading to a frictional-pressure contributions. However, such flow dynamics occur on much longer time scales than the shock waves investigated here.

7. Conclusions

In this work, a hyperbolic macroscale model for high-speed, fully compressible, monodisperse fluid–particle flows with added mass and fluid-phase pseudoturbulence has been developed and tested. The particle-phase equations have been derived from a kinetic model with terms for the collisional, frictional, and pfp-pressure contributions to the particle pressure. The kinetic model accounts as well for the particle-phase internal energy to capture heat transfer with the fluid phase. For simplicity, only velocity moments up to second order are considered in the macroscale model, which is valid for collisional and/or low-Stokes-number flows.

For the numerical solver, the resulting nine-equation macroscale model was discretized with a higher-order method along the lines of the pioneering work of [28]. The two main issue was to adapt the combination of AUSM$^+$up and HLLC initially proposed in the context of a seven-equation, two-fluid model without added mass to the present model and remain stable with higher-order reconstructions using WENO5. This has been done by treating carefully the quantities related to added-mass and the additional non-conservative terms with a consistent discretization. Moreover, the complex coupling of particle- and fluid-phase quantities through the added mass was treated by combining consistently the fluid and particle reconstructions and computing the eigenvalues directly from the Jacobian of the spatial fluxes.

The first numerical study assessed the solver on the mechanical equilibrium and on a challenging gas–particle test case, including a granular phase reaching the packing limit and a strong shock in the fluid phase. The advantages of the proposed method have been showcased in comparison to the first-order HLL scheme used in [22]. Then, the numerical examples presented in the results section demonstrate the capability of the numerical solver to handle a wide range of two-phase systems from supersonic to hypersonic flows, dilute-to-dense granular phases, and gas–particle to bubbly flows. Generally speaking, the macroscale model is able to reproduce the global behavior of PRDNS and experiments from the literature.

In future work, the kinetic-based model and the numerical scheme developed in this work could be extended in several directions. For example, to handle reacting flows, chemical species in the fluid and particle phases can be modeled as done in [27, 28]. Another interesting and important improvement would be to include polydispersity of the particle phase along the lines of the kinetic model developed in [33] and using quadrature-based moments methods for the numerical solver [40]. Finally, in order to simulate the numerous applications involving low-speed, low-Mach-number flows with mean shear, it would be useful to develop a low-Mach-number solver for the macroscale model that neglects the acoustic waves in the fluid phase [43]. For such applications, it will be necessary to include constitutive relations for the viscous and thermal fluxes [4, 8, 9, 30], which have no effect on the hyperbolicity of the macroscale model [22]. These additions would allow the macroscale model to be used for gravity-driven and/or pressure-driven multiphase flows such as bubble columns, sedimentation, and fluidized beds.

Acknowledgments

When preparing this work, ROF was supported by the 2022-2023 Fulbright–Tocqueville Distinguished Chair Award. The Government of the United States or any agency representing it has not endorsed the conclusions or approved the contents of this publication.

Appendix A. Discretized hyperbolic system

This appendix is devoted to the numerical treatment of the hyperbolic system and the consistent reconstruction on cell faces. First, let us write the discrete hyperbolic system for the full model:

$$(\partial_t \alpha_p \rho_p)_i = -\frac{\dot{m}_{p,i+\frac{1}{2}} - \dot{m}_{p,i-\frac{1}{2}}}{\Delta x} \tag{A.1}$$

$$(\partial_t \alpha_p^\star \rho_e)_i = -\frac{\dot{m}^\star_{p,i+\frac{1}{2}} - \dot{m}^\star_{p,i-\frac{1}{2}}}{\Delta x} \tag{A.2}$$

$$(\partial_t \alpha_f^\star \rho_f)_i = -\frac{\alpha^\star_{f,i+\frac{1}{2}} \rho_{f,i+\frac{1}{2}} u_{f,i+\frac{1}{2}} - \alpha^\star_{f,i-\frac{1}{2}} \rho_{f,i-\frac{1}{2}} u_{f,i-\frac{1}{2}}}{\Delta x} \tag{A.3}$$

$$\begin{aligned}(\partial_t \alpha_p^\star \rho_e u_p)_i = &-\frac{\dot{m}^\star_{p,i+\frac{1}{2}} u_{p,i+\frac{1}{2}} + p_{p,i+\frac{1}{2}} - \dot{m}^\star_{p,i-\frac{1}{2}} u_{p,i-\frac{1}{2}} - p_{p,i-\frac{1}{2}}}{\Delta x} \\ &- \alpha^\star_{p,i} \frac{\hat{p}_{f,i+\frac{1}{2}} - \hat{p}_{f,i-\frac{1}{2}}}{\Delta x} - \alpha_{p,i} F_{pf,i} - \frac{P_{pfp,i+\frac{1}{2}} - P_{pfp,i-\frac{1}{2}}}{\Delta x}\end{aligned} \tag{A.4}$$

$$\begin{aligned}(\partial_t \alpha_f^\star \rho_f u_f)_i = &-\frac{\alpha^\star_{f,i+\frac{1}{2}} \rho_{f,i+\frac{1}{2}} u_{f,i+\frac{1}{2}} u_{f,i+\frac{1}{2}} - \alpha^\star_{f,i-\frac{1}{2}} \rho_{f,i-\frac{1}{2}} u_{f,i-\frac{1}{2}} u_{f,i-\frac{1}{2}}}{\Delta x} \\ &- \alpha^\star_{f,i} \frac{\hat{p}_{f,i+\frac{1}{2}} - \hat{p}_{f,i-\frac{1}{2}}}{\Delta x} + \alpha_{p,i} F_{pf,i}\end{aligned} \tag{A.5}$$

$$\begin{aligned}(\partial_t \alpha_p^\star \rho_e K_p)_i = &-\frac{\dot{m}^\star_{p,i+\frac{1}{2}} K_{p,i+\frac{1}{2}} + p_{p,i+\frac{1}{2}} u_{p,i+\frac{1}{2}} - \dot{m}^\star_{p,i-\frac{1}{2}} K_{p,i-\frac{1}{2}} - p_{p,i-\frac{1}{2}} u_{p,i-\frac{1}{2}}}{\Delta x} \\ &- \alpha^\star_{p,i} u_{p,i} \frac{\hat{p}_{f,i+\frac{1}{2}} - \hat{p}_{f,i-\frac{1}{2}}}{\Delta x} - \alpha_{p,i} F_{pf,i} u_{p,i} - u_{p,i} \frac{P_{pfp,i+\frac{1}{2}} - P_{pfp,i-\frac{1}{2}}}{\Delta x}\end{aligned} \tag{A.6}$$

$$(\partial_t \alpha_p^\star \rho_e e_p)_i = -\frac{\dot{m}^\star_{p,i+\frac{1}{2}} e_{p,i+\frac{1}{2}} - \dot{m}^\star_{p,i-\frac{1}{2}} e_{p,i-\frac{1}{2}}}{\Delta x} \tag{A.7}$$

$$\begin{aligned}(\partial_t \alpha_f^\star \rho_f E_f)_i = &-\frac{\alpha^\star_{f,i+\frac{1}{2}} \rho_{f,i+\frac{1}{2}} E_{f,i+\frac{1}{2}} u_{f,i+\frac{1}{2}} - \alpha^\star_{f,i-\frac{1}{2}} \rho_{f,i-\frac{1}{2}} E_{f,i-\frac{1}{2}} u_{f,i-\frac{1}{2}}}{\Delta x} \\ &- \hat{p}_{f,i} \frac{\alpha^\star_{p,i+\frac{1}{2}} u_{p,i+\frac{1}{2}} - \alpha^\star_{p,i-\frac{1}{2}} u_{p,i-\frac{1}{2}}}{\Delta x} - \alpha_{p,i} F_{pf,i} u_{p,i} - P_{pfp,i} \frac{u_{p,i+\frac{1}{2}} - u_{p,i-\frac{1}{2}}}{\Delta x}\end{aligned} \tag{A.8}$$

$$(\partial_t \alpha_f^\star \rho_f k_f)_i = -\frac{\alpha^\star_{f,i+\frac{1}{2}} \rho_{f,i+\frac{1}{2}} k_{f,i+\frac{1}{2}} u_{f,i+\frac{1}{2}} - \alpha^\star_{f,i-\frac{1}{2}} \rho_{f,i-\frac{1}{2}} k_{f,i-\frac{1}{2}} u_{f,i-\frac{1}{2}}}{\Delta x} - \frac{2}{3} \alpha^\star_{f,i} \rho_{f,i} k_{f,i} \frac{u_{f,i+\frac{1}{2}} - u_{f,i-\frac{1}{2}}}{\Delta x} \tag{A.9}$$

Moreover, global mass conservation leads to the following identity:

$$\partial_t(\alpha_p^\star \rho_e + \alpha_f^\star \rho_f) = \partial_t(\alpha_p \rho_p + \alpha_f \rho_f). \tag{A.10}$$

From a discrete perspective, condition eq. (A.10) can only be obtained by properly interpolating quantities at the faces.

By adding eqs. (A.2) and (A.3), and using the definition of $\dot{m}_p^\star$ from eq. (91), we find

$$(\partial_t \alpha_p^\star \rho_e + \partial_t \alpha_f^\star \rho_f)_i = -\frac{\alpha^\star_{p,i+\frac{1}{2}} \rho_{e,i+\frac{1}{2}} u_{p,i+\frac{1}{2}} + \alpha^\star_{f,i+\frac{1}{2}} \rho_{f,i+\frac{1}{2}} u_{f,i+\frac{1}{2}} - \alpha^\star_{p,i-\frac{1}{2}} \rho_{e,i-\frac{1}{2}} u_{p,i-\frac{1}{2}} - \alpha^\star_{f,i-\frac{1}{2}} \rho_{f,i-\frac{1}{2}} u_{f,i-\frac{1}{2}}}{\Delta x}. \tag{A.11}$$

The sum of particle and fluid continuity equations without added-mass (i.e., with $\alpha_a = 0$) gives

$$(\partial_t \alpha_p \rho_p + \partial_t \alpha_f \rho_f)_i = -\frac{\alpha_{p,i+\frac{1}{2}} \rho_p u_{p,i+\frac{1}{2}} + \alpha_{f,i+\frac{1}{2}} \rho_{f,i+\frac{1}{2}} u_{f,i+\frac{1}{2}} - \alpha_{p,i-\frac{1}{2}} \rho_p u_{p,i-\frac{1}{2}} - \alpha_{f,i-\frac{1}{2}} \rho_{f,i-\frac{1}{2}} u_{f,i-\frac{1}{2}}}{\Delta x}. \tag{A.12}$$

At mechanical equilibrium, $u_f = u_p = u_m$ and eq. (A.10) is true discretely if the fluxes are equal at each face:

$$\alpha^\star_{p,i+\frac{1}{2}}\rho_{e,i+\frac{1}{2}}u_m + \alpha^\star_{f,i+\frac{1}{2}}\rho_{f,i+\frac{1}{2}}u_m = \alpha_{p,i+\frac{1}{2}}\rho_p u_m + \alpha_{f,i+\frac{1}{2}}\rho_{f,i+\frac{1}{2}}u_m, \tag{A.13}$$

which leads to a condition on $\alpha^\star_{p,i+\frac{1}{2}}\rho_{e,i+\frac{1}{2}}$:

$$\alpha^\star_{p,i+\frac{1}{2}}\rho_{e,i+\frac{1}{2}} = \alpha_{p,i+\frac{1}{2}}\rho_p + (\alpha_{f,i+\frac{1}{2}} - \alpha^\star_{f,i+\frac{1}{2}})\rho_{f,i+\frac{1}{2}}. \tag{A.14}$$

If the volume-fraction reconstructions are consistent between the particle and fluid phases, then $\alpha^\star_{f,i+\frac{1}{2}} = 1 - \alpha^\star_{p,i+\frac{1}{2}}$ and the following condition can written for $\rho_{e,i+\frac{1}{2}}$:

$$\rho_{e,i+\frac{1}{2}} = \frac{\alpha_{p,i+\frac{1}{2}}}{\alpha^\star_{p,i+\frac{1}{2}}}(\rho_p - \rho_{f,i+\frac{1}{2}}) + \rho_{f,i+\frac{1}{2}}. \tag{A.15}$$

Note that this condition is consistent with the definition of ρ_e in eq. (4).

Appendix B. Analytic integration of source terms

In the numerical method presented in the main text, time splitting is used to solve for the different local source terms. As shown below, this splitting allows to reduce the complex equation system to simple ODEs with analytic solutions. Hence, the potential stability issues due to stiff source terms are avoided.

Appendix B.1. Drag source terms

A semi-analytical solution is used to update the drag terms in the 1-D momentum and energy balances, which amounts to solving the following system of ODEs:

$$\begin{aligned}
\partial_t \rho_f \alpha^\star_f &= 0 \\
\partial_t \rho_e \alpha^\star_p &= 0 \\
\partial_t \rho_f \alpha^\star_f u_f &= \frac{\rho_e \alpha^\star_p}{\tau_p}(u_p - u_f) \\
\partial_t \rho_e \alpha^\star_p u_p &= \frac{\rho_e \alpha^\star_p}{\tau_p}(u_f - u_p) \\
\partial_t \rho_f \alpha^\star_f k_f &= \frac{\rho_e \alpha^\star_p}{\tau_p}[3a\Theta_p - 2(1-a)k_f + u^2_{pf} - C_f k_f] \\
\partial_t \rho_e \alpha^\star_p K_p &= -\frac{\rho_e \alpha^\star_p}{\tau_p}[3a\Theta_p - 2(1-a)k_f + u_{pf}u_p]
\end{aligned}
\quad \Longrightarrow \quad
\begin{aligned}
r &= \frac{\rho_e \alpha^\star_p}{\rho_f \alpha^\star_f} \\
\partial_t(u_f - u_p) &= -\frac{1+r}{\tau_p}(u_f - u_p) \\
\partial_t(u_f + r u_p) &= 0 \\
\partial_t k_f &= \frac{r}{\tau_p}[3a\Theta_p - 2(1-a)k_f] + \frac{r}{\tau_p}[u^2_{pf}(t) - C_f k_f] \\
\partial_t \Theta_p &= \frac{1}{\tau_p}\left[\frac{4}{3}(1-a)k_f - 2a\Theta_p\right]
\end{aligned}
\tag{B.1}$$

with r constant. The particle-phase internal energy e_p does not change due to drag, and the change in fluid-phase total energy $\rho_f \alpha^\star_f E_f$ is determined from conservation of total energy, i.e., $\rho_f \alpha^\star_f E_f + \rho_e \alpha^\star_p E_p$ is constant during drag. Note that the right-hand side for k_f has exchange terms and production/dissipation terms. Each part is handled separately.

Holding τ_p constant over the time step, the updated phase velocities are approximated by

$$\begin{aligned}
u_f(t) - u_p(t) &= (u_f(0) - u_p(0))e^{-(1+r)t/\tau_p} \\
u_f(t) + r u_p(t) &= u_f(0) + r u_p(0)
\end{aligned}
\quad \Longrightarrow \quad
\begin{aligned}
u_f(t) &= \frac{u_f(0)}{1+r}(1 + re^{-(1+r)t/\tau_p}) + \frac{r u_p(0)}{1+r}(1 - e^{-(1+r)t/\tau_p}) \\
u_p(t) &= \frac{u_f(0)}{1+r}(1 - e^{-(1+r)t/\tau_p}) + \frac{u_p(0)}{1+r}(r + e^{-(1+r)t/\tau_p})
\end{aligned}
\tag{B.2}$$

and thus the source term for k_f is given by

$$u^2_{pf}(t) = u^2_{pf}(0)e^{-2(1+r)t/\tau_p}. \tag{B.3}$$

The evolution of $k_f(t)$ is written in two steps. First due to production and dissipation, it is written

$$\hat{k}_f = k_f(0)e^{-C_f rt/\tau_p} + \frac{ru_{pf}^2(0)}{2+(2-C_f)r}\left(e^{-C_f rt/\tau_p} - e^{-2(1+r)t/\tau_p}\right). \tag{B.4}$$

Second, the exchange terms form a linear system:

$$\partial_t \begin{bmatrix} k_f \\ \Theta_p \end{bmatrix} = -\frac{1}{\tau_p}\mathbf{A}\begin{bmatrix} k_f \\ \Theta_p \end{bmatrix} \qquad \text{where} \qquad \mathbf{A} = \begin{bmatrix} 2(1-a)r & -3ar \\ -\frac{4}{3}(1-a) & 2a \end{bmatrix}. \tag{B.5}$$

Since $0 < a_{min} \leq a \leq 1$, the two eigenvalues of $\mathbf{A}$ are non-negative: $\lambda_1 = 0$ and $\lambda_2 = 2r(1-a) + 2a$. Hence, the solution is

$$\begin{aligned} k_f(t) &= \frac{1}{\lambda_2}\left[2r(1-a)\hat{k}_f e^{-\lambda_2 t/\tau_p} + 2a\hat{k}_f + 3ra\Theta_p(0)(1-e^{-\lambda_2 t/\tau_p})\right], \\ \Theta_p(t) &= \frac{1}{\lambda_2}\left[2r(1-a)\Theta_p(0) + 2a\Theta_p(0)e^{-\lambda_2 t/\tau_p} + \frac{4}{3}(1-a)\hat{k}_f(1-e^{-\lambda_2 t/\tau_p})\right]. \end{aligned} \tag{B.6}$$

Note that $2k_f(t)+3r\Theta_p(t) = 2\hat{k}_f+3r\Theta_p(0)$ is constant for the exchange terms, and the parameter a fixes the steady-state value of k_f.

Appendix B.2. Added-mass source terms

A semi-analytical solution is used to handle the 1-D added-mass source terms. For the particle phase, this amounts to solving a linear system of ODEs:

$$\begin{aligned} \partial_t \rho_e \alpha_p^\star &= C_\xi \rho_e \alpha_p^\star \\ \partial_t \rho_e \alpha_p^\star e_p &= C_u e_f \rho_e \alpha_p^\star + (C_\xi - C_u)\rho_e \alpha_p^\star e_p \\ \partial_t \rho_e \alpha_p^\star u_p &= C_u u_f \rho_e \alpha_p^\star + (C_\xi - C_u)\rho_e \alpha_p^\star u_p \\ \partial_t \rho_e \alpha_p^\star K_p &= C_u K_f \rho_e \alpha_p^\star + (C_\xi - C_u)\rho_e \alpha_p^\star K_p \end{aligned} \quad \Longrightarrow \quad \begin{aligned} \partial_t \rho_e \alpha_p^\star &= C_\xi \rho_e \alpha_p^\star \\ \partial_t e_p &= C_u(e_f - e_p) \\ \partial_t u_p &= C_u(u_f - u_p) \\ \partial_t K_p &= C_u(K_f - K_p) \end{aligned} \tag{B.7}$$

with e_f, u_f, K_f, C_ξ, and C_u held constant. The analytical solution for the mass at time t is

$$(\rho_e \alpha_p^\star)(t) = (\rho_e \alpha_p^\star)(0)\, e^{C_\xi t}. \tag{B.8}$$

The change of mass in the fluid phase over the time step Δt is then $(\rho_e \alpha_p^\star)(0) - (\rho_e \alpha_p^\star)(\Delta t)$. For the internal energy, momentum, and kinetic energy, the analytical solutions are

$$e_p(t) = e_p(0)e^{-C_u t} + e_f\left(1 - e^{-C_u t}\right), \tag{B.9}$$

$$u_p(t) = u_p(0)e^{-C_u t} + u_f\left(1 - e^{-C_u t}\right), \tag{B.10}$$

$$K_p(t) = K_p(0)e^{-C_u t} + K_f\left(1 - e^{-C_u t}\right). \tag{B.11}$$

The change in momentum and total energy in the fluid phase are computed in the same manner as for mass. The extension to 3-D flows is done analogously.

Appendix B.3. Heat transfer source term

A semi-analytical solution is used to update the heat transfer in the 1-D energy balances, which amounts to solving the following system of ODEs:

$$\begin{aligned} \partial_t \rho_f \alpha_f^\star &= 0 \\ \partial_t \rho_e \alpha_p^\star &= 0 \\ \partial_t \rho_f \alpha_f^\star E_f &= 6\frac{\alpha_p^\star \lambda_f Nu}{d_p^2}(T_p - T_f) \\ \partial_t \rho_e \alpha_p^\star e_p &= -6\frac{\alpha_p^\star \lambda_f Nu}{d_p^2}(T_p - T_f) \end{aligned} \implies \begin{aligned} r &= \frac{\rho_e \alpha_p^\star C_{p,p} \gamma_f}{\rho_f \alpha_f^\star C_{p,f}} \\ \partial_t (T_f - T_p) &= -(1+r)6\frac{\alpha_p^\star \lambda_f Nu}{d_p^2}(T_f - T_p) \\ \partial_t (T_f + rT_p) &= 0 \end{aligned} \tag{B.12}$$

with r constant. The kinetic energy does not change during heat transfer, hence only internal energy of the fluid and the particles are modified. Conservation of total energy also states that $\rho_f \alpha_f^\star E_f + \rho_e \alpha_p^\star E_p$ is constant during heat transfer.

Holding $C_H = 6\alpha_p^\star \lambda_f Nu / d_p^2$ constant over the time step, the updated phase temperatures are approximated by

$$\begin{aligned} T_f(t) - T_p(t) &= (T_f(0) - T_p(0))e^{-(1+r)\Gamma t} \\ T_f(t) + rT_p(t) &= T_f(0) + rT_p(0) \end{aligned} \implies \begin{aligned} T_f(t) &= \frac{T_f(0)}{1+r}(1 + re^{-(1+r)(1+r)C_H t}) + \frac{rT_p(0)}{1+r}(1 - e^{-(1+r)C_H t}) \\ T_p(t) &= \frac{T_f(0)}{1+r}(1 - e^{-(1+r)C_H t}) + \frac{T_p(0)}{1+r}(r + e^{-(1+r)C_H t}) \end{aligned} \tag{B.13}$$

The updated conservative variables $\rho_f \alpha_f^\star E_f$ and $\rho_e \alpha_p^\star e_p$ are then retrieved from the updated temperatures with $\rho_f \alpha_f^\star$, $\rho_e \alpha_p^\star$, u_f, u_p and k_f constant:

$$\begin{aligned} \rho_f \alpha_f^\star E_f(t) &= \rho_f \alpha_f^\star \left(\frac{1}{2} u_f^2 + \frac{C_{p,f}}{\gamma_f} T_f(t) + k_f \right) \\ \rho_e \alpha_p^\star e_p(t) &= \rho_e \alpha_p^\star C_{p,p} T_p(t) \end{aligned} \tag{B.14}$$

Appendix B.4. Collisional and fricional source terms

A semi-analytical solution is used to update the collisional source terms in the 1-D particle energy balance, which amounts to solving the following system of ODEs:

$$\begin{aligned} \partial_t \rho_e \alpha_p^\star K_p &= -\rho_e \alpha_p^\star \frac{1}{\tau_c}(1 - e_c^2)\Theta_p \\ \partial_t \rho_e \alpha_p^\star e_p &= \rho_e \alpha_p^\star \frac{1}{\tau_c}(1 - e_c^2)\Theta_p \end{aligned} \implies \begin{aligned} \partial_t \Theta_p &= -\frac{2}{3}\frac{1}{\tau_c}(1 - e_c^2)\Theta_p \\ \partial_t e_p &= -\frac{3}{2}\partial_t \Theta_p \end{aligned} \tag{B.15}$$

with τ_c constant. The heating of particles through collision results in a transfer of granular temperature Θ_p to internal energy e_p. Conservation of particle energy states that $\rho_e \alpha_p^\star E_p$ is constant during collisional process. Note that in [28], the integration of the collisional source term takes into account the dependence of τ_c on Θ_p instead of considering τ_c constant during the collisional process.

The updated granular temperature is approximated by

$$\Theta_p(t) = \Theta_p(0) e^{-\frac{2}{3}\frac{(1-e_c^2)}{\tau_c} t} \tag{B.16}$$

The updated energies K_p and e_p are then retrieved from the updated granular temperature with $\rho_e \alpha_p^\star$ and u_p constant:

$$\begin{aligned} K_p(t) &= \rho_e \alpha_p^\star \left(\frac{1}{2} u_p^2 + \frac{3}{2}\Theta_p(t) \right) \\ e_p(t) &= \rho_e \alpha_p^\star \left(e_p(0) - \frac{3}{2}(\Theta_p(t) - \Theta_p(t)) \right) \end{aligned} \tag{B.17}$$

For the frictional source term, the same methodology is used by replacing $\frac{1}{\tau_c}(1 - e_c^2)$ by $\frac{1}{\tau_{fr}}$.

References

[1] P. Batten, N. Clarke, C. Lambert, and D. M. Causon. On the choice of wavespeeds for the HLLC Riemann solver. SIAM Journal on Scientific Computing, 18(6):1553–1570, 1997.

[2] J. Behrendt, S. Balachandar, and T. P. McGrath. Shock interacting with a random array of stationary particles underwater. Physical Review Fluids, 7(2):023401, 2022.

[3] Saad Benjelloun and Jean-Michel Ghidaglia. On the sound speed in two-fluid mixtures and the implications for cfd model validation. European Journal of Mechanics-B/Fluids, 90:152–168, 2021.

[4] D. Berzi, J. T. Jenkins, and P. Richard. Extended kinetic theory for granular flow over and within an inclinded erodible bed. Journal of Fluid Mechanics, 885:A27, 2020.

[5] P. L. Bhatnagar, E. P. Gross, and M. Krook. A model for collision processes in gases. I. Small amplitude processes in charged and neutral one-component systems. Physical Review, 94(3):511, 1954.

[6] J. Capecelatro. Modeling high-speed gas–particle flows relevant to spacecraft landings. International Journal of Multiphase Flow, 150:104008, 2022.

[7] J. Capecelatro and O. Desjardins. An Euler–Lagrange strategy for simulating particle-laden flows. Journal of Computational Physics, 238:1–31, 2013.

[8] J. Chauchat. A comprehensive two-phase flow model for unidirectional sheet-flows. Journal of Hydraulic Research, 56:15, 2018.

[9] J. Chauchat and M. Médale. A three-dimensional numerical model for dense granular flows based on the $\mu(I)$ rheology. Journal of Computational Physics, 256:696–712, 2014.

[10] T. L. Cook and F. H. Harlow. Virtual mass in multiphase flow. International Journal of Multiphase Flow, 10(6):691–699, 1984.

[11] K. A. Daniel and J. L. Wagner. The shock-induced dispersal of particle curtains with varying material density. International Journal of Multiphase Flow, 152:104082, 2022.

[12] S. L. Davis, T. B. Dittmann, G. B. Jacobs, and W. S. Don. Dispersion of a cloud of particles by a moving shock: Effects of the shape, angle of rotation, and aspect ratio. Journal of Applied Mechanics and Technical Physics, 54:900–912, 2013.

[13] E. P. DeMauro, J. L. Wagner, L. J. DeChant, S. J. Beresh, and A. M. Turpin. Improved scaling laws for the shock-induced dispersal of a dense particle curtain. Journal of Fluid Mechanics, 876:881–895, 2019.

[14] A. Di Benedetto, P. Russo, P. Amyotte, and N. Marchand. Modelling the effect of particle size on dust explosions. Chemical Engineering Science, 65(2):772–779, 2010.

[15] B. Einfeldt. On Godunov-type methods for gas dynamics. SIAM Journal on Numerical Analysis, 25(2):294–318, 1988.

[16] B. Einfeldt, C.-D. Munz, P. L. Roe, and B. Sjögreen. On Godunov-type methods near low densities. Journal of Computational Physics, 92(2):273–295, 1991.

[17] R. O. Fox. On multiphase turbulence models for collisional fluid–particle flows. Journal of Fluid Mechanics, 742:368–424, 2014.

[18] R. O. Fox. A kinetic-based hyperbolic two-fluid model for binary hard-sphere collisions. Journal of Fluid Mechanics, 877:282–329, 2019.

[19] R. O. Fox. Advanced approaches in turbulence: Theory, modeling, simulation, and data analysis for turbulent flows, chapter Multiphase turbulence, pages 307–372. Elsevier, Amsterdam, Netherlands, 2021.

[20] R. O. Fox and F. Laurent. Hyperbolic quadrature method of moments for the one-dimensional kinetic equation. SIAM Journal on Applied Mathematics, 82(2):750–771, 2022.

[21] R. O. Fox, F. Laurent, and A. Vié. Conditional hyperbolic quadrature method of moments for kinetic equations. Journal of Computational Physics, 365:269–293, 2018.

[22] R. O. Fox, F. Laurent, and A. Vié. A hyperbolic two-fluid model for compressible flows with arbitrary material-density ratios. Journal of Fluid Mechanics, 903:A5, 2020.

[23] D. Furfaro and R. Saurel. A simple HLLC-type Riemann solver for compressible non-equilibrium two-phase flows. Computers & Fluids, 111:159–178, 2015.

[24] S. Gottlieb, C.-W. Shu, and E. Tadmor. Strong stability-preserving high-order time discretization methods. SIAM Review, 43(1):89–112, 2001.

[25] H. Guillard and B. Nkonga. On the behaviour of upwind schemes in the low Mach number limit: A review. Handbook of Numerical Analysis, 18:203–231, 2017.

[26] D. J. Gunn. Transfer of heat or mass to particles in fixed and fluidized beds. International Journal of Heat and Mass Transfer, 21:467–476, 1978.

[27] R. W. Houim and K. K. Kuo. A low-dissipation and time-accurate method for compressible multi-component flow with variable specific heat ratios. Journal of Computational Physics, 230(23):8527–8553, 2011.

[28] R. W. Houim and E. S. Oran. A multiphase model for compressible granular–gaseous flows: formulation and initial tests. Journal of Fluid Mechanics, 789:166–220, 2016.

[29] K. Huang, H. Wu, H. Yu, and D. Yan. Cures for numerical shock instability in HLLC solver. International Journal for Numerical Methods in Fluids, 65(9):1026–1038, 2011.

[30] J. T. Jenkins and M. Larcher. Dense, steady, fully developed fluid-particle flows over inclined, erodible beds. Physical Review Fluids, 8:024303, 2023.

[31] Guang-Shan Jiang and Chi-Wang Shu. Efficient implementation of weighted eno schemes. Journal of computational physics, 126(1):202–228, 1996.

[32] B. Kong and R. O. Fox. A solution algorithm for fluid–particle flows across all flow regimes. Journal of Computational Physics, 344:575–594, 2017.

[33] B. Kong and R. O. Fox. A moment-based kinetic theory model for polydisperse gas–particle flow. Powder Technology, 365:92–105, 2020.

[34] D. Lhuillier, C.-H. Chang, and T. G. Theofanous. On the quest for a hyperbolic effective-field model of disperse flows. Journal of Fluid Mechanics, 731:184–194, 2013.
[35] Y. Ling, J. L. Wagner, S. J. Beresh, S. P. Kearney, and S. Balachandar. Interaction of a planar shock wave with a dense particle curtain: Modeling and experiments. Physics of Fluids, 24(11):113301, 2012.
[36] M.-S. Liou. A sequel to AUSM: AUSM$^+$. Journal of Computational Physics, 129(2):364–382, 1996.
[37] M.-S. Liou. A sequel to AUSM, Part II: AUSM$^+$-up for all speeds. Journal of Computational Physics, 214(1):137–170, 2006.
[38] M.-S. Liou and C. J. Steffen Jr. A new flux splitting scheme. Journal of Computational Physics, 107(1):23–39, 1993.
[39] E. Loth, J. Tyler Daspit, M. Jeong, T. Nagata, and T. Nonomura. Supersonic and hypersonic drag coefficients for a sphere. AIAA Journal, 59(8):3261–3274, 2021.
[40] D. L. Marchisio and R. O. Fox. Computational Models for Polydisperse Particulate and Multiphase Systems. Cambridge University Press, Cambridge, UK, 2013.
[41] T. McGrath, J. St. Clair, and S. Balachandar. Modeling compressible multiphase flows with dispersed particles in both dense and dilute regimes. Shock Waves, 28:533–544, 2018.
[42] M. Mehrabadi, S. Tenneti, R. Garg, and S. Subramaniam. Pseudo-turbulent gas-phase velocity fluctuations in homogeneous gas-solid flow: fixed particle assemblies and freely evolving suspensions. Journal of Fluid Mechanics, 770:210–246, 2015.
[43] A. Passalacqua and R. O. Fox. Implementation of an interative solution procedure for multi-fluid gas–particle flow models on unstructured grids. Powder Technology, 213(1):174–187, 2011.
[44] A. Passalacqua, J. E. Galvin, P. Vedula, C. M. Hrenya, and R. O. Fox. A quadrature-based kinetic model for dilute non-isothermal granular flows. Communications in Computational Physics, 10(01):216–252, 2011.
[45] M. Pelanti and R. J. LeVeque. High-resolution finite volume methods for dusty gas jets and plumes. SIAM Journal on Scientific Computing, 28(4):1335–1360, 2006.
[46] X. Rogue, G. Rodriguez, J. F. Haas, and R. Saurel. Experimental and numerical investigation of the shock-induced fluidization of a particles bed. Shock Waves, 8(1):29–45, 1998.
[47] R. Saurel and R. Abgrall. A simple method for compressible multifluid flows. SIAM Journal on Scientific Computing, 21(3):1115–1145, 1999.
[48] S. Serna and A. Marquina. Capturing shock waves in inelastic granular gases. Journal of Computational Physics, 209(2):787–795, 2005.
[49] G. S. Shallcross, R. O. Fox, and J. Capecelatro. A volume-filtered description of compressible particle-laden flows. International Journal of Multiphase Flow, 122:103138, 2020.
[50] R. J. Spiteri and S. J. Ruuth. A new class of optimal high-order strong-stability-preserving time discretization methods. SIAM Journal on Numerical Analysis, 40(2):469–491, 2002.
[51] T. G. Theofanous, V. Mitkin, and C.-H. Chang. The dynamics of dense particle clouds subjected to shock waves. Part 1. Experiments and scaling laws. Journal of Fluid Mechanics, 792:658–681, 2016.
[52] E. F. Toro, M. Spruce, and W. Speares. Restoration of the contact surface in the HLL-Riemann solver. Shock Waves, 4(1):25–34, 1994.
[53] A. Vié, F. Doisneau, and M. Massot. On the anisotropic Gaussian velocity closure for inertial-particle laden flows. Communications in Computational Physics, 17(01):1–46, 2015.
[54] J. L. Wagner, K. Daniel, C. Downing, T. W. Grasser, and K. P. Lynch. Shock–particle-curtain interactions at high Mach number. In AIAA SCITECH 2023 Forum, page 2303, 2023.
[55] M. Wang, Y. Yang, D. Z. Zhang, and S. Balachandar. Numerical calculation of the particle–fluid–particle stress in random arrays of fixed particles. Physical Review Fluids, 6:104306, 2021.
[56] F. Zhang, D. L. Frost, P. A. Thibault, and S. B. Murray. Explosive dispersal of solid particles. Shock Waves, 10(6):431–443, 2001.